Computational Flow Analysis in Aerospace, Energy and Transportation Technologies with the Variational Multiscale Methods

Kenji TAKIZAWA[1], *Yuri BAZILEVS*[2], *Tayfun E. TEZDUYAR*[1,3,*], *Artem KOROBENKO*[4]

[1]Waseda University, Tokyo, Japan
[2]Brown University, Providence, Rhode Island, USA
[3]Rice University, Houston, Texas, USA
[4]University of Calgary, Calgary, Alberta, Canada

*Corresponding Author: Tayfun E. TEZDUYAR (Email: tezduyar@tafsm.org)
(Received: 14-Feb-2020; accepted: 21-Feb-2020; published: 30-Jun-2020)
DOI: http://dx.doi.org/10.25073/jaec.202042.279

Abstract. *With the recent advances in the variational multiscale (VMS) methods, computational flow analysis in aerospace, energy and transportation technologies has reached a high level of sophistication. It is bringing solution in challenging problems such as aerodynamics of parachutes, thermo-fluid analysis of ground vehicles and tires, and fluid–structure interaction (FSI) analysis of wind turbines. The computational challenges include complex geometries, moving boundaries and interfaces, FSI, turbulent flows, rotational flows, and large problem sizes. The Residual-Based VMS (RBVMS), Arbitrary Lagrangian-Eulerian VMS (ALE-VMS) and Space–Time VMS (ST-VMS) methods have been successfully serving as core methods in addressing the computational challenges. The core methods are supplemented with special methods targeting specific classes of problems, such as the Slip Interface (SI) method, Multi-Domain Method, and the "ST-C" data compression method. We provide and overview of the core and special methods. We present, as examples of challenging computations performed with these methods, aerodynamic analysis of a ram-air parachute, thermo-fluid analysis of a freight truck and its rear set of tires, and aerodynamic and FSI analysis of two back-to-back wind turbines in atmospheric boundary layer flow.*

Keywords

Aerospace technologies, Energy technologies, Transportation technologies, Computational flow analysis, FSI, Space–Time VMS method, ALE-VMS method

1. Introduction

With the recent advances in the variational multiscale (VMS) methods, computational flow analysis in aerospace, energy and transportation technologies has reached a high level of sophistication. It is bringing solution in many classes of challenging problems. Examples are spacecraft parachute analysis for the landing-stage parachutes [1], cover-separation parachutes [2] and the drogue parachutes [3], spacecraft aerodynamics [2], ram-air parachutes [4], compressible-flow spacecraft parachute aerodynamics [5], thermo-fluid analysis of ground vehicles and their tires [6], flow around tires with road contact and deformation [7], thermo-

fluid analysis of disk brakes [8], flow analysis of turbocharger turbines [9], wind-turbine aerodynamics and fluid–structure interaction (FSI) [10], more specifically, vertical-axis wind turbines [11], floating wind turbines [12], wind turbines in atmospheric boundary layer (ABL) flow [13], and fatigue damage in wind-turbine blades [14]. The computational challenges encountered in these classes of problems include complex geometries, moving boundaries and interfaces (MBI), FSI, turbulent flows, rotational flows, and large problem sizes.

1.1. Methods

Our core methods in addressing the computational challenges are the Residual-Based VMS (RBVMS) [15–18], ALE-VMS [19–25] and Space–Time VMS (ST-VMS) [6, 26, 27]. methods. We supplement the core methods with a number of special methods targeting specific classes of problems. The special methods used in combination with the ST-VMS include the ST Slip Interface (ST-SI) method [8, 28], ST Isogeometric Analysis (ST-IGA) [26, 29, 30], Multi-Domain Method (MDM) [31], and the "ST-C" data compression method [32]. The special methods used in combination with the ALE-VMS include weak enforcement of no-slip boundary conditions [33–35] and "sliding interfaces" [36, 37] (the acronym "SI" will also indicate that).

We will provide an overview of the core and special methods and present examples of challenging computations performed with these methods. Much of the material presented in this review article has been extracted from [38] and the earlier articles written by the authors.

1.2. Examples of the challenging computations performed

1) Aerodynamic analysis of a ram-air parachute

This computation is from [4]. A ram-air parachute is a parafoil inflated by the airflow through the inlets at the leading edge. The parafoil behaves like a wing and has better control and gliding capability compared to a round parachute. Its usage is quite common in sports parachuting and special-purpose parachuting that requires good gliding control and landing precision. Their usage is less common at larger sizes, and experience with their design, testing and performance evaluation becomes less and less as the size increases. Wind tunnel testing is not an option for very large ram-air parachutes, and drop tests would be very costly. That generated a demand for computational analysis and motivated the development of methods for reliable analysis (see, for example, [39]).

Reliable analysis of ram-air parachutes, at any practical size, involves a number of computational challenges. They include accurate representation of the parafoil geometry, fabric porosity and the complex, multiscale flow behavior encountered in this class of problems. The FSI between the parachute and the airflow is another computational challenge, with the challenge level increasing with the parachute size. Ram-air parachute computations were the earliest reported 3D, coupled parachute aerodynamics and parachute dynamics computations [40] with the ST-SUPS, and among the earliest reported 3D parachute FSI computations [39] with the ST-SUPS.

Here we use the ST-VMS and ST-SI-IGA. We use a special-purpose NURBS mesh generation techniques for the parachute structure and the flow field inside and outside the parafoil. The special-purpose mesh generation techniques enable NURBS representation of the structure and fluid domains with significant geometric complexity. The test computations we present from [4] are for building a starting parachute shape and a starting flow field associated with that parachute shape, which are the first two key steps in FSI analysis.

2) Thermo-fluid analysis of a freight truck and its rear set of tires

This computation is from [6]. Increasing the accuracy in calculating the heat transfer rates

from the tires is the main objective. The multiscale challenges are due to the turbulent nature of the flow and due to the tires being rather small compared to the entire truck. The thermo-fluid–structure analysis of a tire is very complex. Here, we assume that the tire temperature is given. This assumption is justified because the tire temperature depends on the driving history, which represents a much longer time scale compared to the time scale of the surrounding air. To make the point, the truck body is 12 m long, and at a driving speed of 80 km/h, a fluid particle takes only 0.54 s to travel the full length of the truck. With that, we can decouple the problem into thermo-fluid analysis and tire thermo-structure analysis. Here we focus only on the thermo-fluid part.

In our thermo-fluid analysis, the road-surface temperature is higher than the free-stream temperature, and the tire-surface temperature is even higher. The analysis includes the heat from the engine and exhaust system. This is done with a reasonably realistic representation of the rate by which that heat transfer takes place and the surface geometry of the engine and exhaust system over which the heat transfer takes place. The analysis also includes the heave motion of the truck body, prescribed as a periodic motion with a given semi-amplitude and frequency.

3) Aerodynamic and FSI analysis of two back-to-back HAWTs in turbulent ABL flow

This computation is from [41]. To obtain high-fidelity predictive simulation results for wind turbines, 3D modeling is essential. However, simulation of wind turbines at full scale engenders a number of challenges. The flow is fully turbulent, requiring highly accurate methods and increased grid resolution. The presence of boundary layers, where turbulence is created, complicates the situation further. Wind-turbine blades are long and slender structures, with complex distribution of material properties, for which the numerical approach must have good efficiency and approximation power, and avoid locking. Wind-turbine simulations involve moving and stationary components, and the fluid–structure coupling must be accurate, efficient and robust to preclude divergence of the computations.

Additional modeling challenges stem from realistic scenarios of wind turbines arranged in arrays, and operating in complex turbulent ABL flows with a wide range of energy-containing scales and in different atmospheric stability regimes. Wind turbines positioned downstream operate in the wakes generated by upstream turbines, and have been observed to generate less power compared to the upstream turbines. In addition, downstream turbines experience higher variations in aerodynamic loads, which tend to shorten their fatigue life, leading to premature blade failure. Depending on the atmospheric stability regime, spacing between turbines, the underlying surface topology, turbulence intensity, and wind direction and speed, the power-generation deficit for the downstream turbines may be as high as 40%.

We adopt the MDM technique to carry out the aerodynamic and FSI simulations of two full-scale, back-to-back HAWTs operating in a stably stratified ABL. The simulations produce novel data for the rotor structural response as it operates in shear flow induced by thermal stratification. The simulations also clearly show the evolution of the upstream-turbine wake leading to a velocity deficit responsible for a 15% drop in the downstream-turbine efficiency.

1.3. Outline of the remaining sections

We provide the governing equations in Section 2. The core and special methods are described in Sections 3–11. In Sections 12 and 13, as examples of ST computations, we present aerodynamic analysis of a ram-air parachute and thermo-fluid analysis of a freight truck and its rear set of tires. In Section 14, as an example of ALE computations, we present aerodynamic and FSI simulations of two full-scale, back-to-back HAWTs operating in a stably stratified ABL. The concluding remarks are given in Section 15.

2. Governing equations

2.1. Incompressible flow with thermal coupling

The Navier–Stokes equations of incompressible flows with thermal coupling and Boussinesq approximation and the thermal-transport (energy) equation can be written on the spatial domain Ω_t as

$$\rho\left(\frac{\partial \mathbf{u}}{\partial t}+\mathbf{u}\cdot\boldsymbol{\nabla}\mathbf{u}-\mathbf{f}\right)-\boldsymbol{\nabla}\cdot\boldsymbol{\sigma}=\mathbf{0}, \tag{1}$$

$$\boldsymbol{\nabla}\cdot\mathbf{u}=0, \tag{2}$$

$$\rho C_{\mathrm{p}}\left(\frac{\partial \theta}{\partial t}+\mathbf{u}\cdot\boldsymbol{\nabla}\theta\right)-\boldsymbol{\nabla}\cdot(\kappa\boldsymbol{\nabla}\theta)=0, \tag{3}$$

where

$$\rho\mathbf{f}=\rho\left(1-\beta_\theta\left(\theta-\theta_{\mathrm{ref}}\right)\right)\mathbf{a}_{\mathrm{GRAV}}. \tag{4}$$

In the momentum equation, ρ, $\mathbf{u}$ and $\mathbf{f}$ are the density, velocity and body force. The stress tensor $\boldsymbol{\sigma}(\mathbf{u},p)=-p\mathbf{I}+2\mu\boldsymbol{\varepsilon}(\mathbf{u})$, where p is the pressure, $\mathbf{I}$ is the identity tensor, $\mu=\rho\nu$ is the viscosity, ν is the kinematic viscosity, and the strain rate $\boldsymbol{\varepsilon}(\mathbf{u})=\left(\boldsymbol{\nabla}\mathbf{u}+(\boldsymbol{\nabla}\mathbf{u})^T\right)/2$. In the energy equation, C_{p}, θ and κ are the constant-pressure specific heat, temperature and thermal conductivity. In the expression for the body force, β_θ, θ_{ref} and $\mathbf{a}_{\mathrm{GRAV}}$ are the thermal-expansion coefficient, reference temperature and gravitational acceleration. In this mathematical model, ρ and C_{p} are assumed to be constants.

The essential and natural boundary conditions associated with Eq. (1) are represented as $\mathbf{u}=\mathbf{g}$ on $(\Gamma_t)_g$ and $\mathbf{n}\cdot\boldsymbol{\sigma}=\mathbf{h}$ on $(\Gamma_t)_h$, where $(\Gamma_t)_g$ and $(\Gamma_t)_h$ are complementary subsets of the boundary Γ_t, $\mathbf{n}$ is the unit outward normal vector, and $\mathbf{g}$ and $\mathbf{h}$ are given functions. The essential and natural boundary conditions associated with Eq. (3) are represented as $\theta=g_\theta$ on $(\Gamma_t)_{g_\theta}$, and $\kappa\mathbf{n}\cdot\boldsymbol{\nabla}\theta=\mathbf{q}$ on $(\Gamma_t)_{h_\theta}$, where $(\Gamma_t)_{g_\theta}$ and $(\Gamma_t)_{h_\theta}$ are complementary subsets of the boundary Γ_t, and g_θ and $\mathbf{q}$ are given functions.

Remark 1. *If the space "1" in Eq. (4) is omitted, then p represents the pressure after the static-fluid part at θ_{ref} is subtracted.*

In deriving the multiscale ST formulation associated with Eqs. (1)–(3), we find it more convenient to start from the conservation-law form of the momentum and energy equations:

$$\frac{\partial(\rho\mathbf{u})}{\partial t}+\boldsymbol{\nabla}\cdot(\mathbf{u}\rho\mathbf{u})-\rho\mathbf{f}-\boldsymbol{\nabla}\cdot\boldsymbol{\sigma}=\mathbf{0}, \tag{5}$$

$$\frac{\partial(\rho C_{\mathrm{p}}\theta)}{\partial t}+\boldsymbol{\nabla}\cdot(\mathbf{u}\rho C_{\mathrm{p}}\theta)-\boldsymbol{\nabla}\cdot(\kappa\boldsymbol{\nabla}\theta)=0. \tag{6}$$

2.2. Structural mechanics

In this article we will not provide any of our formulations requiring fluid and structure definitions simultaneously; we will instead give reference to earlier journal articles where the formulations were presented. Therefore, for notation simplicity, we will reuse many of the symbols used in the fluid mechanics equations to represent their counterparts in the structural mechanics equations. To begin with, $\Omega_t\subset\mathbb{R}^{n_{\mathrm{sd}}}$ and Γ_t will represent the structure domain and its boundary. The structural mechanics equations are then written, on Ω_t and $\forall t\in(0,T)$, as

$$\rho\left(\frac{\mathrm{d}^2\mathbf{y}}{\mathrm{d}t^2}-\mathbf{f}\right)-\boldsymbol{\nabla}\cdot\boldsymbol{\sigma}=\mathbf{0}, \tag{7}$$

where $\mathbf{y}$ and $\boldsymbol{\sigma}$ are the displacement and Cauchy stress tensor. The essential and natural boundary conditions for Eq. (7) are represented as $\mathbf{y}=\mathbf{g}$ on $(\Gamma_t)_{\mathrm{g}}$ and $\mathbf{n}\cdot\boldsymbol{\sigma}=\mathbf{h}$ on $(\Gamma_t)_{\mathrm{h}}$. The Cauchy stress tensor can be obtained from

$$\boldsymbol{\sigma}=J^{-1}\mathbf{F}\cdot\mathbf{S}\cdot\mathbf{F}^T, \tag{8}$$

where $\mathbf{F}$ and J are the deformation gradient tensor and its determinant, and $\mathbf{S}$ is the second Piola–Kirchhoff stress tensor. It is obtained from the strain-energy density function φ as follows:

$$\mathbf{S}\equiv\frac{\partial\varphi}{\partial\mathbf{E}}, \tag{9}$$

where $\mathbf{E}$ is the Green–Lagrange strain tensor:

$$\mathbf{E}=\frac{1}{2}\left(\mathbf{C}-\mathbf{I}\right), \tag{10}$$

and $\mathbf{C}$ is the Cauchy–Green deformation tensor:

$$\mathbf{C}\equiv\mathbf{F}^T\cdot\mathbf{F}. \tag{11}$$

From Eqs. (9) and (10),

$$\mathbf{S} = 2\frac{\partial \varphi}{\partial \mathbf{C}}. \tag{12}$$

3. ST-VMS and ST-SUPS

The ST-VMS and ST-SUPS are versions of the Deforming-Spatial-Domain/Stabilized ST (DSD/SST) method [42–44], which was introduced for computation of flows with moving boundaries and interfaces (MBI), including FSI. The ST-SUPS is a new name for the original version of the DSD/SST, with "SUPS" reflecting its stabilization components, the Streamline-Upwind/Petrov-Galerkin (SUPG) [45] and Pressure-Stabilizing/Petrov-Galerkin (PSPG) [42] stabilizations. The ST-VMS is the VMS version of the DSD/SST. The VMS components of the ST-VMS are from the residual-based VMS (RBVMS) method [15–18]. The five stabilization terms of the ST-VMS include the three that the ST-SUPS has, and therefore the ST-VMS subsumes the ST-SUPS. In MBI computations the ST-VMS and ST-SUPS function as a moving-mesh methods. Moving the fluid mechanics mesh to follow an interface enables mesh-resolution control near the interface and, consequently, high-resolution boundary-layer representation near fluid–solid interfaces. Because of the higher-order accuracy of the ST framework (see [26,27]), the ST-SUPS and ST-VMS are desirable also in computations without MBI.

The ST-SUPS and ST-VMS have been applied to many classes of challenging FSI, MBI and fluid mechanics problems (see [46] for a comprehensive summary of the computations prior to July 2018). The classes of problems include spacecraft parachute analysis for the landing-stage parachutes [1, 22, 47–49], cover-separation parachutes [2] and the drogue parachutes [3, 50, 51], wind-turbine aerodynamics for horizontal-axis wind-turbine rotors [22, 52–54], full horizontal-axis wind-turbines [55–58] and vertical-axis wind-turbines [28, 59, 60], flapping-wing aerodynamics for an actual locust [22, 29, 61, 62], bioinspired MAVs [56, 57, 63, 64] and wing-clapping [65, 66], blood flow analysis of cerebral aneurysms [56, 67], stent-blocked aneurysms [67–69], aortas [70–74], heart valves [57,65,72,74–80] and coronary arteries in motion [81], spacecraft aerodynamics [2, 82], thermo-fluid analysis of ground vehicles and their tires [6, 76], thermo-fluid analysis of disk brakes [8], flow-driven string dynamics in turbomachinery [83–85], flow analysis of turbocharger turbines [9,30,86–88], flow around tires with road contact and deformation [7,76,89–91], fluid films [91,92], ram-air parachutes [4], and compressible-flow spacecraft parachute aerodynamics [5, 93].

For more on the ST-VMS and ST-SUPS, see [22]. In the flow analyses presented here, the ST framework provides higher-order accuracy in a general context. The VMS feature of the ST-VMS addresses the computational challenges associated with the multiscale nature of the unsteady flow. The moving-mesh feature of the ST framework enables high-resolution computation near the truck body as it undergoes heave motion.

4. ALE-VMS, RBVMS and ALE-SUPS

The ALE-VMS [19–25] is the VMS version of the ALE [94]. It succeeded the ST-SUPS [42] and ALE-SUPS [39] and preceded the ST-VMS. The VMS components are from the RBVMS [15–18]. It is the moving-mesh extension of the RBVMS formulation of incompressible turbulent flows proposed in [17], and as such, it was first presented in [19] in the FSI context. The ALE-SUPS, RBVMS and ALE-VMS have also been applied to many classes of challenging FSI, MBI and fluid mechanics problems. The classes of problems include ram-air parachute FSI [39], wind-turbine aerodynamics and FSI [10, 41, 52, 58–60, 95–99], more specifically, vertical-axis wind turbines [11, 59, 60, 100], floating wind turbines [12], wind turbines in atmospheric boundary layers [13, 41, 59, 60], and fatigue damage in wind-turbine blades [14], patient-specific cardiovascular fluid mechanics and FSI [19, 101–106], biomedical-device FSI [107–112], ship hydrodynamics with free-surface flow and fluid–object interaction [113,114], hydrodynamics and FSI of a hydraulic arresting gear [115, 116],

hydrodynamics of tidal-stream turbines with free-surface flow [117], passive-morphing FSI in turbomachinery [118], bioinspired FSI for marine propulsion [119, 120], bridge aerodynamics and fluid–object interaction [121–123], and mixed ALE-VMS/Immersogeometric computations [110–112, 124, 125] in the framework of the Fluid–Solid Interface-Tracking/Interface-Capturing Technique [126]. Recent advances in stabilized and multiscale methods may be found for stratified incompressible flows in [127], for divergence-conforming discretizations of incompressible flows in [128], and for compressible flows with emphasis on gas-turbine modeling in [129].

For more on the ALE-VMS, RBVMS and ALE-SUPS, see [22]. In the flow analyses presented here, the VMS feature of the ALE-VMS addresses the computational challenges associated with the multiscale nature of the unsteady flow. The moving-mesh feature of the ALE framework enables high-resolution computation near the wind-turbine blades.

5. ALE-SI and ST-SI

The ALE-SI was introduced in [36, 37] to retain the desirable moving-mesh features of the ALE-VMS in computations with spinning solid surfaces, such as a turbine rotor. The mesh covering the spinning surface spins with it, retaining the high-resolution representation of the boundary layers. The method was in the context of incompressible-flow equations. Interface terms added to the ALE-VMS to account for the compatibility conditions for the velocity and stress at the SI accurately connect the two sides of the solution. The ST-SI was introduced in [28], also in the context of incompressible-flow equations, to retain the desirable moving-mesh features of the ST-VMS and ST-SUPS in computations with spinning solid surfaces. The starting point in its development was the ALE-SI. Interface terms similar to those in the ALE-SI are added to the ST-VMS to accurately connect the two sides of the solution. An ST-SI version where the SI is between fluid and solid domains was also presented in [28]. The SI in this case is a "fluid–solid SI" rather than a standard "fluid–fluid SI" and enables weak enforcement of the Dirichlet boundary conditions for the fluid. The ST-SI introduced in [8] for the coupled incompressible-flow and thermal-transport equations retains the high-resolution representation of the thermo-fluid boundary layers near spinning solid surfaces. These ST-SI methods have been applied to aerodynamic analysis of vertical-axis wind turbines [28,59,60], thermo-fluid analysis of disk brakes [8], flow-driven string dynamics in turbomachinery [83–85], flow analysis of turbocharger turbines [9, 30, 86–88], flow around tires with road contact and deformation [7, 76, 89–91], fluid films [91, 92], aerodynamic analysis of ram-air parachutes [4], and flow analysis of heart valves [72, 74, 77–80].

In another ST-SI version presented in [28] the SI is between a thin porous structure and the fluid on its two sides. This enables dealing with the porosity in a fashion consistent with how the standard fluid–fluid SIs are dealt with and how the Dirichlet conditions are enforced weakly with fluid–solid SIs. This version also enables handling thin structures that have T-junctions. This method has been applied to incompressible-flow aerodynamic analysis of ram-air parachutes with fabric porosity [4]. The compressible-flow ST-SI methods were introduced in [5], including the version where the SI is between a thin porous structure and the fluid on its two sides. Compressible-flow porosity models were also introduced in [5]. These, together with the compressible-flow ST SUPG method [130], extended the ST computational analysis range to compressible-flow aerodynamics of parachutes with fabric and geometric porosities. That enabled ST computational flow analysis of the Orion spacecraft drogue parachute in the compressible-flow regime [5,93].

For more on the ST-SI, see [8,28]. In the computations here, with the ALE-SI we are able to handle the interaction between the spinning rotor and stationary tower. The ST-SI enables dealing with the fabric porosity of the ram-air parachute. The porosity velocity is expressed as a function of the pressure difference between the two sides of the SI. The expression can take different forms depending on the nature of the porosity. Here we use the form given in [4]. The normal component of the velocity is assumed to

be continuous, and the tangential component is set to the tangential component of $\mathbf{u}_{\mathrm{S}}^{h}$, where $\mathbf{u}_{\mathrm{S}}^{h}$ is the structure velocity, and the volume flux is imposed with the porosity velocity taken into account (see [4] for the complete set of equations).

6. Stabilization parameters

The ST-SUPS, ALE-SUPS, RBVMS, ALE-VMS and ST-VMS all have some embedded stabilization parameters that play a significant role (see [22]). These parameters involve a measure of the local length scale (also known as "element length") and other parameters such as the element Reynolds and Courant numbers. There are many ways of defining the stabilization parameters. Some of the newer options for the stabilization parameters used with the SUPS and VMS can be found in [6,7,28,29,54,55,131–134]. Some of the earlier stabilization parameters used with the SUPS and VMS were also used in computations with other SUPG-like methods, such as the computations reported in [118,135–146]. The stabilization-parameter definitions used in the computations reported in this article can be found from the references cited in the sections where those computations are described.

7. Discontinuity-capturing term

The thermo-fluid analysis methods based on the SUPG/PSPG formulation of the coupled incompressible-flow and thermal-transport equations were presented in [44]. The methods were described in the ALE context since the description followed a section on the ALE formulation with SUPG and PSPG stabilizations and a reader who sees the methods in the ALE context can easily imagine them in the ST context. The methods presented in [44] included discontinuity-capturing (DC) options for both sets of equations as well as stabilization and DC parameters for the thermal-transport equation. The options for the DC parameters were based on those introduced with the "DCDD stabilization" [43, 147, 148] and "YZβ shock-capturing" [149–151]. These thermo-fluid analysis methods were successfully used in [152] in a number of 2D test computations as well as in a 3D computation with a simplified model of air circulation and cooling in a small data center. A new element length scale option applicable to the stabilization parameters for both the incompressible-flow and thermal-transport equations were introduced in [6]. The new length scale option is applicable also to the DC parameter for the thermal-transport equation.

In the flow analyses presented here, we use the YZβ shock-capturing in the thermo-fluid analysis of a freight truck and its rear set of tires. We use it for the for the thermal-transport equation. The DC parameter is a slightly modified version of the one given in [44], which was based on the DC parameter introduced with the YZβ shock-capturing, with the element length scale option introduced in [6]. The modification is as given in [6].

8. ST-IGA

The ST-IGA is the integration of the ST framework with isogeometric discretization, motivated by the success of NURBS meshes in spatial discretization [19, 36, 101, 153]. It was introduced in [26]. Computations with the ST-VMS and ST-IGA were first reported in [26] in a 2D context, with IGA basis functions in space for flow past an airfoil, and in both space and time for the advection equation. Using higher-order basis functions in time enables getting full benefit out of using higher-order basis functions in space (see the stability and accuracy analysis given in [26] for the advection equation).

The ST-IGA with IGA basis functions in time enables, as pointed out and demonstrated in [26, 27, 29, 61, 63], a more accurate representation of the motion of the solid surfaces and a mesh motion consistent with that. It also enables more efficient temporal representation of the motion and deformation of the volume meshes, and more efficient remeshing. These motivated the development of the STNMUM [29,55,61,63]. The STNMUM has a wide scope that includes spinning solid surfaces. With

the spinning motion represented by quadratic NURBS in time, and with sufficient number of temporal patches for a full rotation, the circular paths are represented exactly. A "secondary mapping" [22, 26, 27, 29] enables also specifying a constant angular velocity for invariant speeds along the circular paths. The ST framework and NURBS in time also enable, with the "ST-C" method, extracting a continuous representation from the computed data and, in large-scale computations, efficient data compression [6, 8, 32, 76, 83–85]. The STNMUM and the ST-IGA with IGA basis functions in time have been used in many 3D computations. The classes of problems solved are flapping-wing aerodynamics for an actual locust [22, 29, 61, 62], bioinspired MAVs [56, 57, 63, 64] and wing-clapping [65, 66], separation aerodynamics of spacecraft [2], aerodynamics of horizontal-axis [55–58] and vertical-axis [28, 59, 60] wind-turbines, thermo-fluid analysis of ground vehicles and their tires [6, 76], thermo-fluid analysis of disk brakes [8], flow-driven string dynamics in turbomachinery [83–85], flow analysis of turbocharger turbines [9, 30, 86–88], and flow analysis of coronary arteries in motion [81].

The ST-IGA with IGA basis functions in space enables more accurate representation of the geometry and increased accuracy in the flow solution. It accomplishes that with fewer control points, and consequently with larger effective element sizes. That in turn enables using larger time-step sizes while keeping the Courant number at a desirable level for good accuracy. It has been used in ST computational flow analysis of turbocharger turbines [9, 30, 86–88], flow-driven string dynamics in turbomachinery [84, 85], ram-air parachutes [4], spacecraft parachutes [93], aortas [72–74], heart valves [72, 74, 77–80], coronary arteries in motion [81], tires with road contact and deformation [7, 90, 91], and fluid films [91, 92]. Using IGA basis functions in space is now a key part of some of the newest arterial zero-stress-state (ZSS) estimation methods [74, 154–159] and related shell analysis [160].

For more on the ST-IGA, see [4, 22, 30, 61]. In the computational flow analyses presented here, the ST-IGA enables more accurate representation of the ram-air parachute geometry, increased accuracy in the flow solution, and using larger time-step sizes. Integration of the ST-SI with the ST-IGA enables dealing with the fabric porosity of the ram-air parachute, and we will describe the ST-SI-IGA in Section 9.

9. ST-SI-IGA

The ST-SI-IGA is the integration of the ST-SI and ST-IGA. The turbocharger turbine flow [9, 30, 86–88] and flow-driven string dynamics in turbomachinery [84, 85] were computed with the ST-SI-IGA. The IGA basis functions were used in the spatial discretization of the fluid mechanics equations and also in the temporal representation of the rotor and spinning-mesh motion. That enabled accurate representation of the turbine geometry and rotor motion and increased accuracy in the flow solution. The IGA basis functions were used also in the spatial discretization of the string structural dynamics equations. That enabled increased accuracy in the structural dynamics solution, as well as smoothness in the string shape and fluid dynamics forces computed on the string.

The ram-air parachute analysis [4] and spacecraft parachute compressible-flow analysis [93] were conducted with the ST-SI-IGA, based on the ST-SI version that weakly enforces the Dirichlet conditions and the ST-SI version that accounts for the porosity of a thin structure. The ST-IGA with IGA basis functions in space enabled, with relatively few number of unknowns, accurate representation of the parafoil and parachute geometries and increased accuracy in the flow solution. The volume mesh needed to be generated both inside and outside the parafoil. Mesh generation inside was challenging near the trailing edge because of the narrowing space. The spacecraft parachute has a very complex geometry, including gores and gaps. Using IGA basis functions addressed those challenges and still kept the element density near the trailing edge of the parafoil and around the spacecraft parachute at a reasonable level.

In the heart valve analysis [72, 74, 77–80], the ST-SI-IGA, beyond enabling a more accurate representation of the geometry and increased accuracy in the flow solution, kept the element

density in the narrow spaces near the leaflet contact areas at a reasonable level.

In computational analysis of flow around tires with road contact and deformation [7, 90, 91], the ST-SI-IGA enables a more accurate representation of the geometry and motion of the tire surfaces, a mesh motion consistent with that, and increased accuracy in the flow solution. It also keeps the element density in the tire grooves and in the narrow spaces near the contact areas at a reasonable level. In addition, we benefit from the mesh generation flexibility provided by using SIs. In computational analysis of fluid films [91, 92], the ST-SI-IGA enabled solution with a computational cost comparable to that of the Reynolds-equation model for the comparable solution quality [92]. With that, narrow gaps associated with the road roughness [91] can be accounted for in the flow analysis around tires.

An SI provides mesh generation flexibility in a general context by accurately connecting the two sides of the solution computed over nonmatching meshes. This type of mesh generation flexibility is especially valuable in complex-geometry flow computations with isogeometric discretization, removing the matching requirement between the NURBS patches without loss of accuracy. This feature was used in the flow analysis of heart valves [72, 74, 77–80], turbocharger turbines [9, 30, 86–88], and spacecraft parachute compressible-flow analysis [93].

For more on the ST-SI-IGA, see [4]. In the computations presented here, the ST-SI-IGA is used for the reasons given and as described in the first paragraph of this section.

10. ST-C

The ST-C [32], which serves here as a data compression method in large-scale computations, is based on continuous temporal representation of the computed data using NURBS basis functions, with the letter "C" indicating "continuous." As we compute the flow field, we store the computed time-dependent data with the ST-C. With the ST-C, we can represent the data with fewer temporal control points, resulting in reduced computer storage cost. In one of the two ST-C versions introduced in [32], the continuous representation is extracted by projection from a solution already computed. Because we use a successive-projection technique (SPT), with a small number of temporal NURBS basis functions at each projection, the extraction can take place as the original solution is being computed, without the need to first complete the computation and store all that data. This version was named "ST-C-SPT" in [32]. The ST-C, as a data compression method, was used in a number computations (see [6, 8, 76, 83–85]), with applications ranging from multiscale thermo-fluid analysis of a ground vehicle and its tires to thermo-fluid analysis of a disk brake, to flow-driven string dynamics in turbomachinery.

For more on the ST-C, see [32]. In the flow analyses presented here, the ST-C-SPT is used in the thermo-fluid analysis of a freight truck and its rear set of tires. The large time-history data from the thermo-fluid computation over the global domain of the MDM is stored using the ST-C-SPT. The stored data is used in the thermo-fluid computation over the local domain containing the rear set of tires.

11. MDM

The MDM [31] was introduced for flow computations where the purpose is to predict the long-wake flow generated by a primary object and, in some cases, also to determine the influence of this wake flow on a secondary object placed far downstream. In the MDM, the problem domain is divided into a sequence of overlapping subdomains. The primary object is placed in the primary subdomain. The subsequent subdomains are used for computing the long-wake flows and flow past secondary objects. The inflow-boundary condition for the primary subdomain is the free-stream velocity. The inflow-boundary condition for each a subsequent subdomain is the velocity extracted from the subdomain preceding it. If the outflow boundary of a subsequent subdomain is also within the subdomain preceding it, then the stress condition there is also extracted from the preceding subdomain. Computations over subdomains with no object can be carried out with special, struc-

tured meshes or special flow solvers that take into account the special nature of the mesh or with completely different flow solvers.

The 3D applications of the MDM method included flow around a small wing placed in the wake of a larger wing [31], flow in the wake of a circular cylinder up to 300 diameters downstream [161], aerodynamics [162] and FSI [163]. of a parachute crossing the far wake of an aircraft In the case of the cylinder problem, at Reynolds number 140, it was shown that with the MDM the computations can be extended sufficiently downstream, and with sufficient accuracy, to successfully capture the second phase of the Karman vortex street observed in laboratory experiments. In the case of the parachute crossing the aircraft wake, the computations were based on the DSD/SST method, and the subdomain containing the parachute was fully inside the subdomain preceding it.

In this article we use a spatially multiscale version of the MDM in the thermo-fluid analysis of a freight truck and its rear set of tires. The full global domain serves as the primary subdomain, and the local domain containing the rear set of tires serves as the secondary subdomain. In this version, the secondary subdomain is fully inside the primary subdomain. First the thermo-fluid computation is carried out over the global domain, with a reasonable mesh refinement. The inflow-boundary conditions are the free-stream velocity and temperature, the outflow-boundary conditions are zero stress and zero normal heat flux, and the conditions at the top and side computational boundaries are zero normal velocity, zero tangential stress and zero normal heat flux. The large amount of time-history data from the global computation is stored using the ST-C-SPT (see Section 10).

This is followed by a higher-resolution computation over the local domain. This gives us increased accuracy in the thermo-fluid analysis, including increased accuracy in the heat transfer rates from the tires. The boundary conditions at the inflow and top and side computational boundaries at each time step of the computation are the velocity and temperature extracted from the stored global data at the corresponding time. The extraction is based on evaluating the temporal NURBS representation of the velocity at that corresponding time. At the outflow boundary, the stress condition is extracted from the stored global data, and the normal heat flux is set to zero. In general the nodal points of the local-domain boundaries do not coincide with the nodal points of the global domain. Therefore, spatially, the data extraction is based on the least-squares projection. If a local-domain boundary coincides with the global-domain boundary, the boundary condition there is from the values specified for the global domain.

The MDM is also used in this article in the aerodynamic and FSI analysis of two back-to-back wind turbines in ABL flow. It is used in the way the MDM was originally conceived, with the two wind turbines serving as primary and secondary objects.

12. ST computation: aerodynamic analysis of a ram-air parachute

This computation is from [4].

12.1. Structural mechanics computation

A ram-air parachute consists of three parts: canopy, suspension lines, and stabilizers. Figure 1 shows the parachute. The canopy size is approximately 8×3 m^2. The canopy is made of fabric, which is modeled as membrane, with 19 airfoil-shaped ribs, 17 separating the air cells and 2 at the ends. Figure 2 shows one of the ribs. The suspension lines, used by the parachutist to control the parachute, are modeled as cables. Fabric patches attached to the parachute sides serve as stabilizers.

Figure 3 shows the undeformed configuration, where the membrane parts consist of mostly flat patches. We note that in the configuration we selected, the suspension lines have not yet been reeled in.

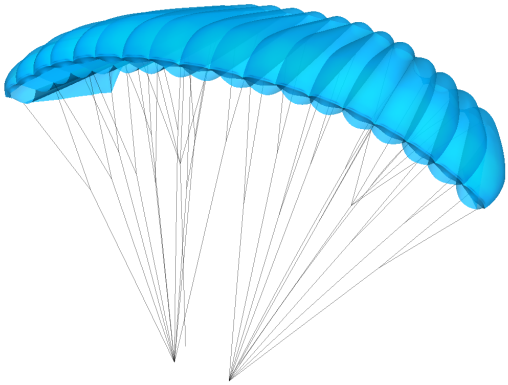

Fig. 1: Ram-air parachute.

Fig. 2: One of the ribs.

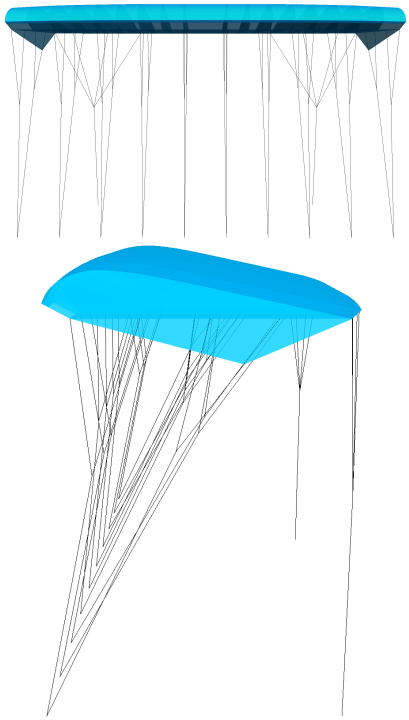

Fig. 3: Undeformed geometry. Front (*top*) and side (*bottom*) views.

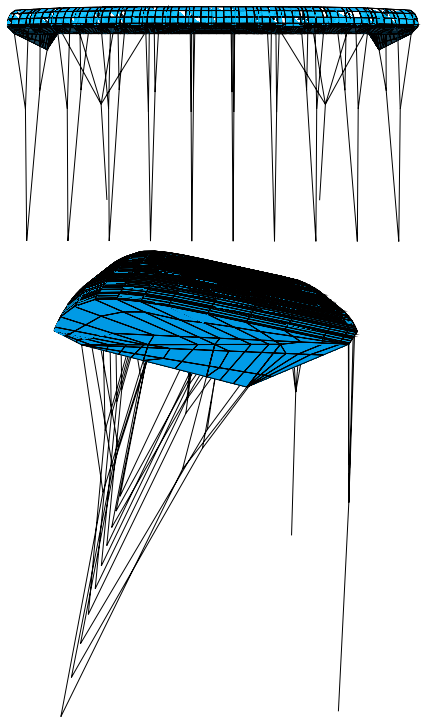

Fig. 4: Undeformed control mesh. Front (*top*) and side (*bottom*) views.

Figure 4 shows the control mesh in the NURBS representation of the undeformed configuration. To represent such a complex shape or to add a cable attached to a surface, some control points coalesce (see Figure 5). Because of the coalescing, at some element boundaries we have only C^0 continuity. The number of control points is 3,296, with 2,250 elements in the membrane parts and 222 elements in the cables. We use quadratic NURBS.

The structural mechanics formulation based on the membrane and cable models (see [1]) is

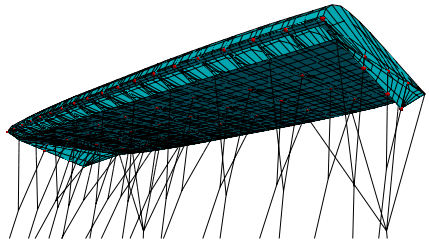

Fig. 5: Undeformed control mesh with *red* spheres representing the control points that coalesced.

Tab. 1: Material properties.

	Membrane	Cable
Young's modulus (Pa)	3.8×10^{8}	7.6×10^{10}
Density (kg/m^3)	5.0×10^{2}	1.4×10^{3}
Poisson's ratio	0.3	-
Thickness (in)	3×10^{-3}	-
Cross-section area (mm^2)	-	8.0

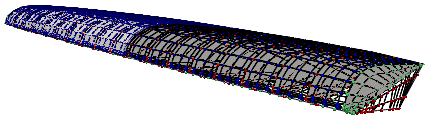

Fig. 6: Pressure difference for the control points of the canopy structure mesh. Surface membranes have been removed in the *right* half of the picture to make the ribs visible. The values are, in Pa, 0 (*red*), 94.1 (*green*) and 117 (*blue*).

supplemented with wrinkling and slacking models (see [164]). The material properties are given in Table 1.

In the computation, we specify the pressure difference between the two sides of the parafoil surfaces and reel the ends of the suspension lines to the center. Figure 6 shows the pressure difference for the control points of the canopy structure mesh. We have three different values, and they are, in Pa, 0, 94.1 and 117. The stress vector is formed based on the control variables, using the surface normal and interpolated value at each surface location.

The structural mechanics solution is symmetrized with respect to the central vertical plane by averaging. In addition, we apply an upward body force to keep the parachute in an upright position. The solution is obtained by computing with a time-marching algorithm until a steady state is reached.

Figure 7 shows, for the steady-state solution, the control mesh and the surface represented by that mesh.

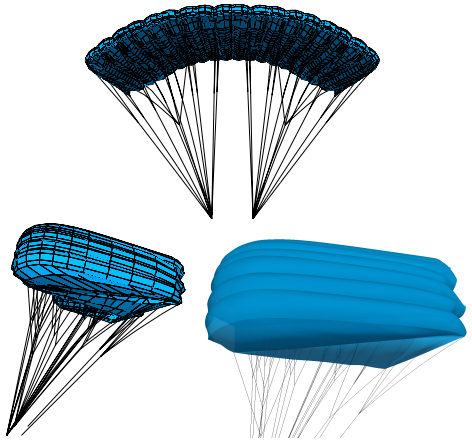

Fig. 7: Deformed configuration at the steady state. Control mesh and surface represented by that mesh.

12.2. Fluid mechanics computations

The density and kinematic viscosity are 1.237 kg/m^3 and 1.449×10^{-5} m^2/s. The glide speed is 12.5 m/s. The computational-domain size is $100\times100\times100$ m^3. The parachute is located at 30 m from the inflow boundary.

The surface mesh is the same as the canopy structural mechanics mesh. The volume mesh needs to be generated both inside and outside the parafoil. Mesh generation inside is challenging near the trailing edge because of the narrowing space. Using NURBS meshes for the fluid mechanics computation addresses that challenge. This keeps the element density near the trailing edge at a reasonable level. We create the volume mesh in two steps: first we generate a mesh using the undeformed parafoil shape, which is relatively easier, and then deform that mesh as the parafoil deforms in the structural mechanics computation. Figure 8 shows the mesh obtained in these two steps. The number of control points and elements are 149,568 and 233,378. We use quadratic NURBS.

To represent the pressure jump across a parafoil surface, the control variables on the surfaces have split values. The mesh deformation is computed with the Jacobian-based stiffening method [165]. Volume meshes for different values of the angle of attack (α), ranging from

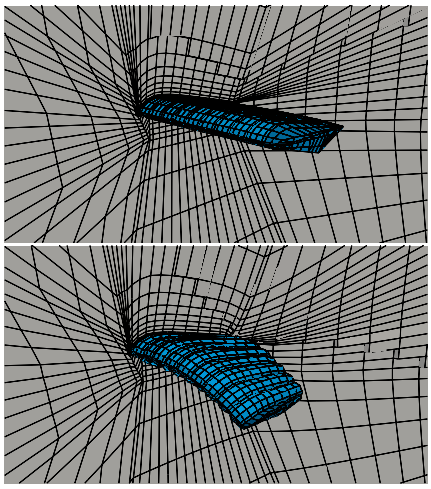

Fig. 8: Fluid mechanics control mesh before (*top*) and after (*bottom*) the structural deformation.

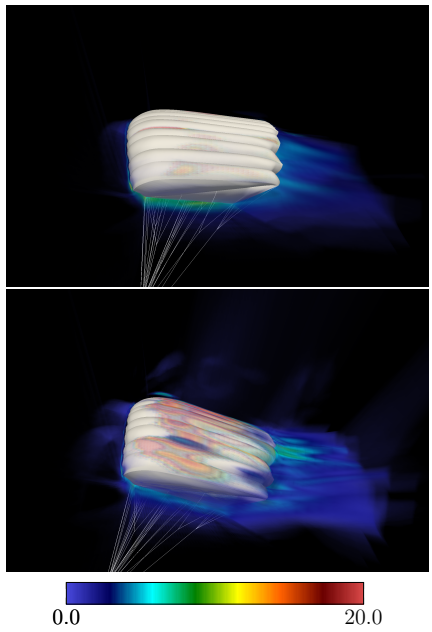

Fig. 9: Vorticity magnitude (s^{-1}) at an instant for $\alpha = 0°$ (*top*) and 12° (*bottom*).

$-2.0°$ to 12°, are obtained by deforming the mesh for $\alpha = 0°$, and the deformation is driven by the rotation of the parachute canopy from $\alpha = 0°$ to the other values of α.

At the inflow boundary we set the velocity, based on the glide speed, to 12.5 m/s, and at the outflow boundary we set the stress to zero. We use slip conditions at the lateral boundaries, and no-slip condition on the parafoil surfaces. We use the ST-VMS method. For the stabilization parameters used, see [4]. The time-step size is 5.34×10^{-3} s, and the number of nonlinear iterations per time step is 3. The number of GMRES [166] iterations per nonlinear iteration is 300.

Figure 9 shows the vorticity at an instant for $\alpha = 0°$ and 12°. Despite the coarseness of the meshes, the solutions are smooth and capture well the attached flow when $\alpha = 0°$ and the separated flow when $\alpha = 12°$. Figures 10 and 11 show the pressure coefficient at an instant for $\alpha = -2°$, 0°, 2°, 4°, 6°, 8°, 10°, and 12°. The picture plane is cutting the 9th cell from the right, roughly bisecting it. The scaling used in computing the pressure coefficient gives a value of 1.0 as the stagnation (i.e. maximum) pressure. Figure 12 shows the moment coefficient around the parachutist and the lift/drag ratio. For each α value, the data displayed was obtained by averaging from the last 2.5 s of the computation.

For $\alpha = 0°$, we also compute the flow field with porosity at all parafoil surfaces except for the top canopy surface. The porosity coefficient is 1.5 CFM. At the top canopy surface, we enforce the no-slip condition weakly. Figure 13 shows the vorticity at an instant. Figure 14 shows the normal component of the velocity at an instant.

13. ST computation: thermo-fluid analysis of a freight truck and its rear set of tires

This computation is from [6].

13.1. Problem setup

Figure 15 shows the truck model and the dimensions. For the tire, the diameter: 1.07 m, and width: 0.35 m. The number of rear tires is 8. For other tire-related dimensions, see [6]. The truck is moving at 80 km/h, and with that, the free-

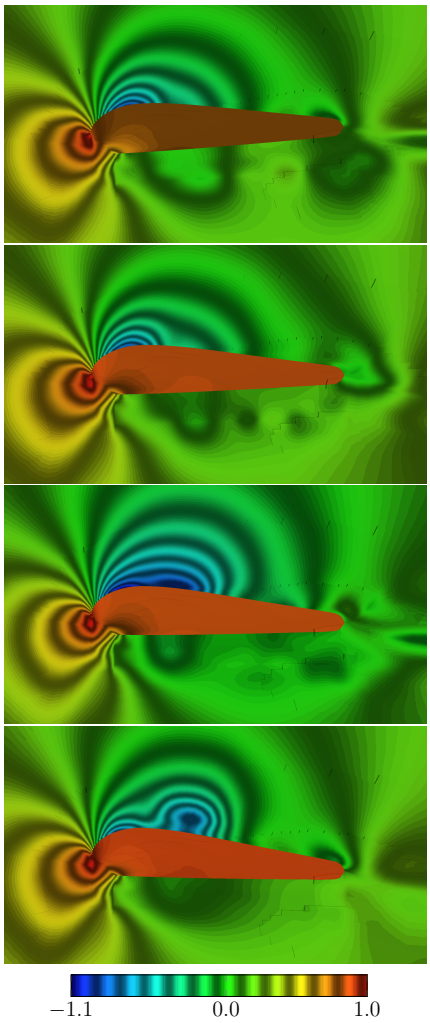

Fig. 10: Pressure coefficient at an instant for $\alpha = -2°$, $0°$, $2°$, and $4°$.

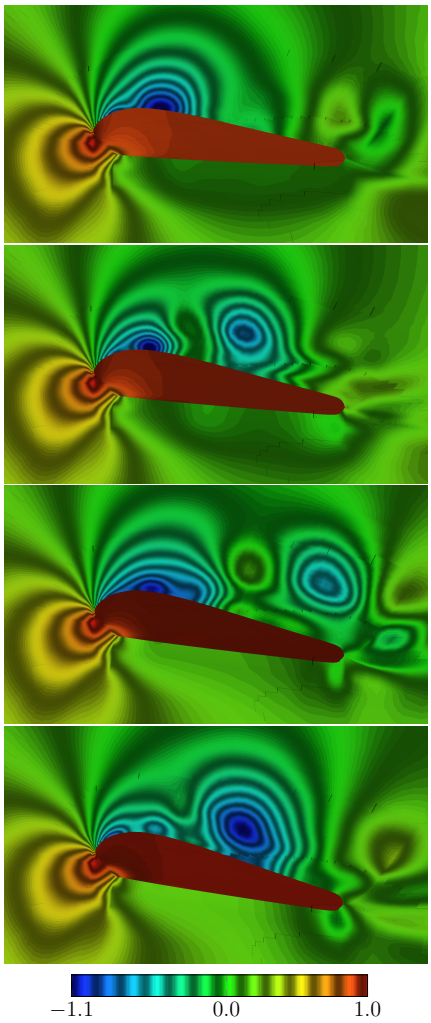

Fig. 11: Pressure coefficient at an instant for $\alpha = 6°$, $8°$, $10°$, and $12°$.

stream velocity for the computational domain is 80 km/h. The road surface moves in the computational domain with the same speed. The rotational velocity for the tire can be calculated from the truck speed and tire diameter (see [6]). The tires have axial symmetry in the computation, and therefore we do not need a moving mesh to represent the rotation. However, we model the truck-body heave motion, and for that we use a moving mesh. For details of the heave motion, see [6]. Figure 16 shows the global domain and its size. For details on the thermo-fluid properties and boundary conditions used in the computation, including how the thermal boundary conditions were estimated, see [6]. Figure 17 shows the three heat loss locations, which play a role in those estimates.

The local domain contains the left half of the rear tires. Figure 18 shows how it was placed. Figure 19 shows the size of the local domain. The boundary conditions for the local domain, which come from the boundary conditions and computed values of the global domain, are specified according to the approach described in Section 11. For details, see [6].

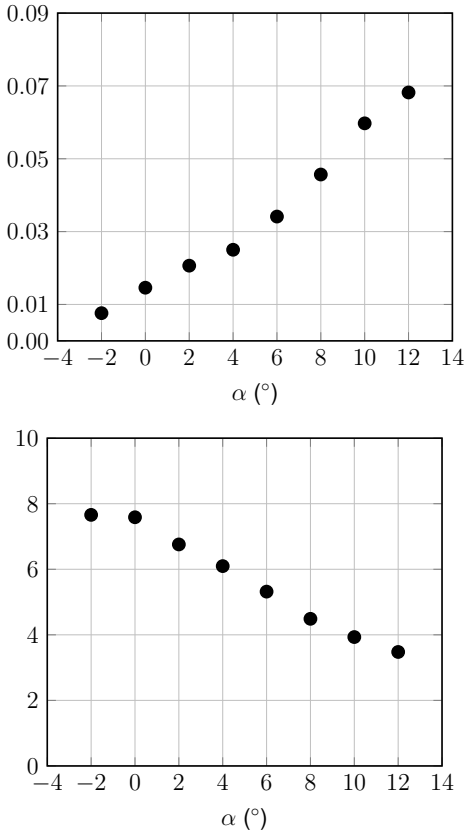

Fig. 12: Moment coefficient (*top*) and lift/drag ratio (*bottom*).

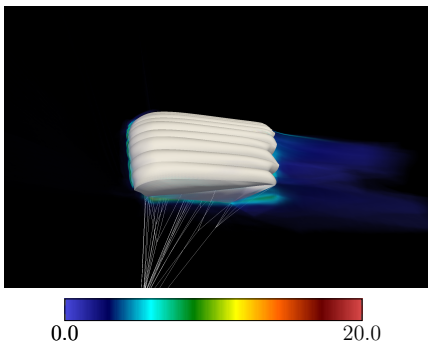

Fig. 13: Computation with porosity. Vorticity magnitude (s^{-1}) at an instant for $\alpha = 0°$.

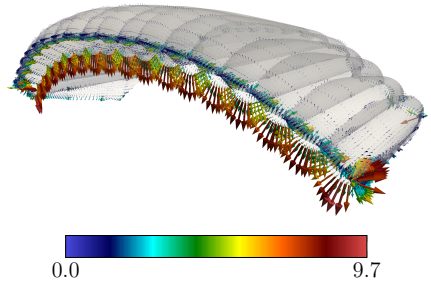

Fig. 14: Computation with porosity. Normal component of the velocity (m/s) at an instant for $\alpha = 0°$.

Fig. 15: Truck model. Length: 12.14 m, width: 2.41 m, height: 3.77 m.

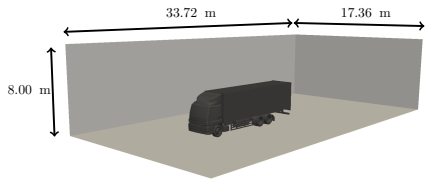

Fig. 16: Global domain.

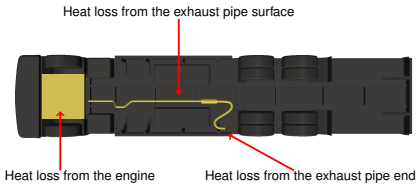

Fig. 17: Heat loss locations used in specifying the boundary conditions.

Fig. 18: Local domain containing the left half of the rear tires.

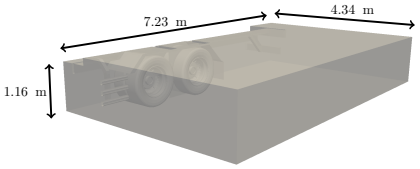

Fig. 19: Size of the local domain.

Tab. 2: Number of nodes (nn) and elements (ne) in the global and local meshes.

	nn	ne
Global domain	918,753	4,857,973
Local domain	5,809,813	32,986,249

13.2. Computations and results

The number of nodes and elements in the global and local meshes, which were both generated with tetrahedral elements, are given in Table 2. There are approximately 58 million unknowns in the computation over the local domain. The mesh near the tire is shown in Figure 20. For more on the mesh, see [6].

The global computation is based one the ST-SUPS, and the local computation, ST-VMS. For the stabilization parameters and the other computational conditions, see [6]. For how we store the computed data from the global domain with the ST-C-SPT, how we represent the heave motion, and how we move the mesh, see [6]. The duration of the global computation is 1.56 s. The local computation starts at 0.52 s and ends at 1.56 s.

Figures 21 and 22 show the temperature at an instant from the global and local computations. Figure 23 shows the Nusselt number at an instant from the local computation and the time-history of the spatially-averaged Nusselt number from the global and local computations. Figure 24 shows the time- and circumferentially-averaged Nusselt number from the global and local computations. All tire-specific results reported are for the outer leading tire. Details on how the heat transfer coefficient and Nusselt number are calculated and how the circumferential averaging is done can be found in [6].

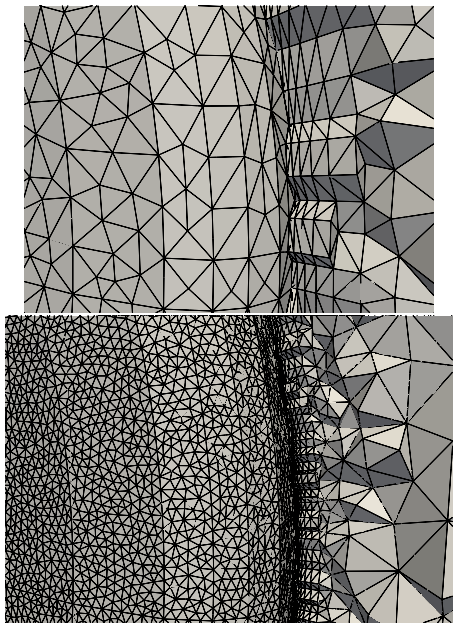

Fig. 20: Mesh resolution in the tangential and normal directions for the global and local domains.

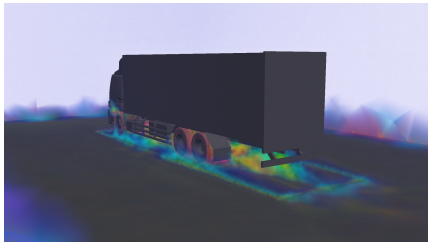

Fig. 21: Temperature (°C) at $t = 1.04$ s from the global computation. Color range from *blue* to *red* corresponds to the temperature range from low to high.

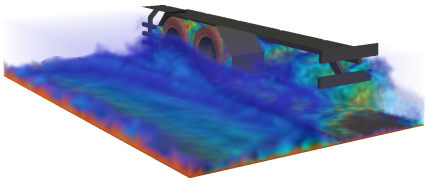

Fig. 22: Temperature (°C) at $t = 1.04$ s from the local computation. Color range from *blue* to *red* corresponds to the temperature range from low to high.

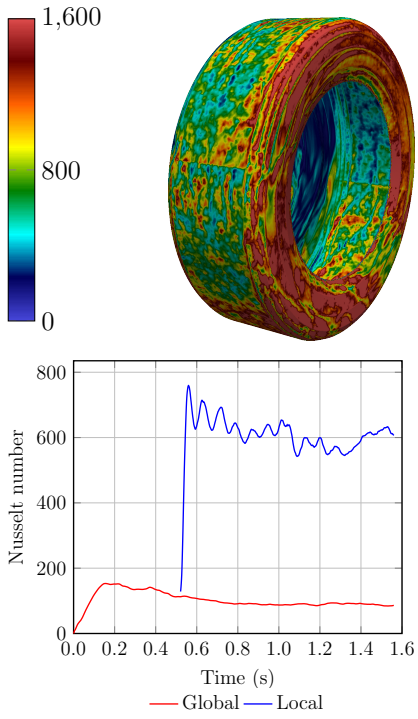

Fig. 23: Nusselt number at $t = 1.04$ s from the local computation and time-history of the spatially-averaged Nusselt number from the global and local computations.

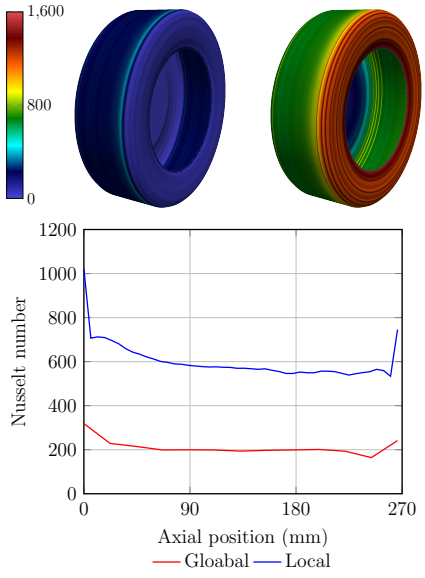

Fig. 24: Time- and circumferentially-averaged Nusselt number from the global (*left*) and local (*center*) computations and the profiles (*right*) in the axial direction.

14. ALE computation: aerodynamic and FSI analysis of two back-to-back HAWTs in turbulent ABL flow

This computation is from [41].

In this section, the techniques described are applied to the simulation of two back-to-back NREL 5 MW wind turbines [167] operating in ABL flow. Each turbine has a rotor with 61 m blades mounted on an 80 m tower and operating at constant, fixed rotor speed of 9 rpm. This rotor speed gives the optimal tip-speed ratio for 8 m/s wind [167], which is also the geostrophic wind speed used in the present computations. The material presented in this section is taken from [41].

14.1. Computational setup and boundary conditions

Two wind turbines are positioned one behind the other at a distance of 480 m, which corresponds to four rotor diameters. The wake generated by the upstream turbine needs to be accurately computed over a long domain before it impacts the downstream turbine, which poses a significant computational challenge due to a very large problem size. To circumvent this difficulty, the MDM (see Section 11) is adopted in the present work to efficiently separate the two turbine domains.

In the present work the MDM is employed as follows. The problem domain is divided into three subdomains (see Figure 25 for dimensions and notation). Domains labeled *Turbine 1* and *Turbine 2* contain the upstream and downstream turbines, respectively, and domain labeled *Box* contains the space between the turbines. The three domains are simulated in a sequential manner. Velocity and temperature boundary conditions at the inflow boundary of *Turbine 1*, as well as lateral boundaries of all subdomains, are obtained from a standalone 3D LES computation of a stratified ABL with a

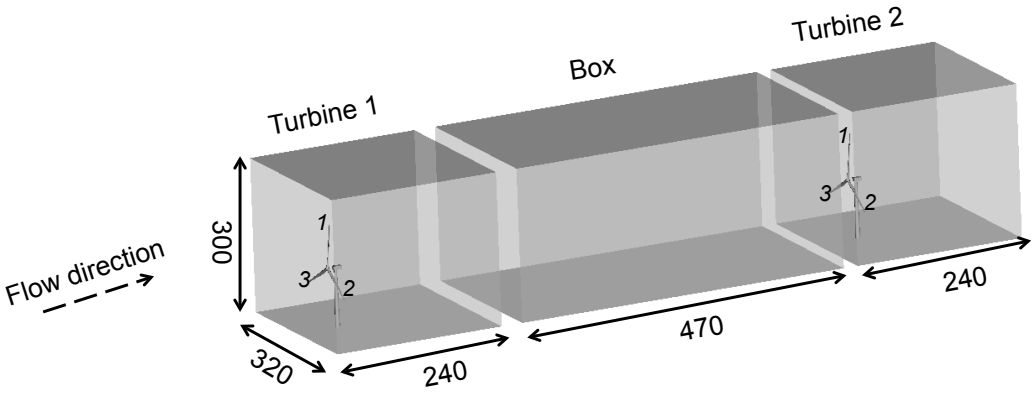

Fig. 25: The three subdomains in the MDM wind-turbine simulation. Dimensions are in m.

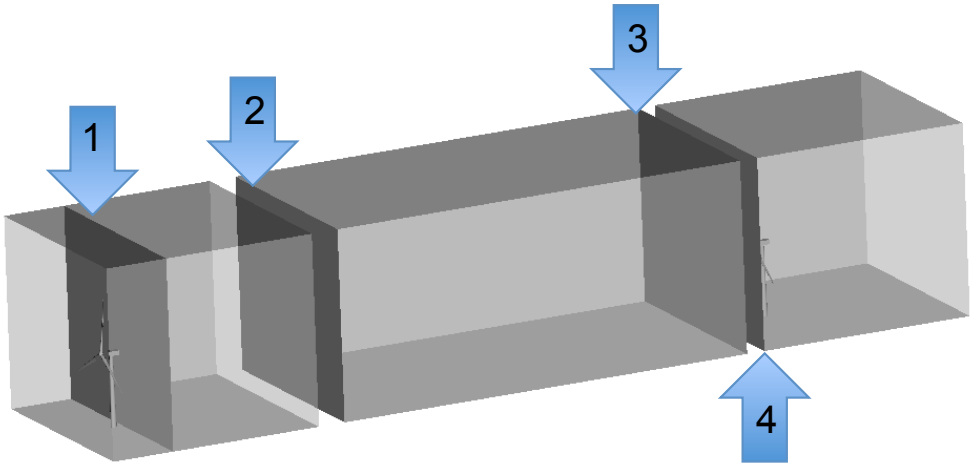

Fig. 26: Data flow between the subdomains. Velocity and temperature collected at location 1 are applied as inlet boundary conditions at location 2. Velocity and temperature collected at location 3 are applied as inlet boundary conditions at location 4. At all lateral boundaries velocity and temperature boundary conditions come from a standalone spectral/fine-difference LES.

uniform grid size of 5 m. This stratified flow computational model [168], which can be run in DNS or LES modes, makes use of a mixed spectral/finite-difference algorithm and a subgrid model based on dynamic eddy viscosity and diffusivity. Nodal values of the velocity and temperature boundary conditions are obtained by interpolating the finite-difference solution from the structured grid of the LES simulation to the unstructured grids of the wind-turbine simulations. This data transfer strategy, employing the same dataset as in the present work, was successfully tested for the rotor-only ABL simulation in [13]. The background temperature $\bar{\theta}$ is set to 260 K up to 100 m with an overlying inversion of strength 0.01 K/m for all domains. The geostrophic wind speed is set to 8 m/s, and the Coriolis parameter to $f_c = 1.39\times10^{-4}$. Velocity and temperature inflow boundary conditions for *Box* are obtained using a similar data transfer strategy, where, in this case, the data is obtained by interpolating the solution on a plane positioned 10 m behind the turbine during pure aerodynamic simulation on *Turbine 1*. Inflow boundary conditions for *Turbine 2* are obtained by interpolating the solution on the outflow plane of *Box* (see Figure 26 for details.)

Traction boundary conditions are prescribed at the outlet boundaries of all subdomains. To

generate the traction values, a simulation in *Turbine 1* is performed first with the wind turbine removed, and with zero outlet traction boundary conditions. The inlet tractions produced as a result of this computation, shown in Figure 27, are then assigned as outlet boundary conditions for all subdomains. A similar strategy was successfully employed in [13], as well as in [6] to perform a detailed thermo-fluid analysis of the rear tires of a ground vehicle.

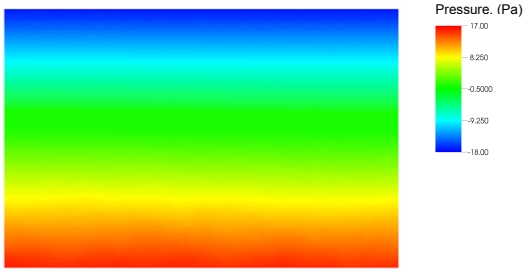

Fig. 27: Pressure profile used at the outflow boundary of all subdomains.

The subdomains are discretized using triangular prisms in the boundary layer region near the wind-turbine rotors, and tetrahedra elsewhere (see Figure 28). For *Turbine 1* and *Turbine 2* the boundary-layer mesh design is based on that reported in [10]. For *Turbine 1* a total of 7,824,602 elements are used with a 4 m element length on the outer boundaries. A finer grid resolution with 2 m element length is used on a plane behind the upstream turbine where inlet data is collected for the *Box* simulation. The *Box* domain, which has a refined inner region to more accurately represent the wake turbulence, is discretized using 15,436,631 elements The *Turbine 2*, with a total of 9,153,426 elements, also contains a refined inner region in front of the turbine for better resolution. The time step size is set to 10^{-4} s for the *Turbine 1* and *Turbine 2* simulations, and to 10^{-2} s for the *Box* simulation.

14.2. Aerodynamics simulation

Pure aerodynamics simulation results, which are also referred as "CFD," are reported in this section. During the CFD simulations the wind turbine rotor is considered as a rigid body. Figure 29 shows the velocity and temperature contours on the domain center plane. No discernible discontinuity between the subdomains is observed. A slight growth of the shear layer from the upper edge of the upstream-turbine rotor can also be seen in Figure 29. The bottom shear layer grows much more rapidly, due to higher turbulent mixing and presence of the tower.

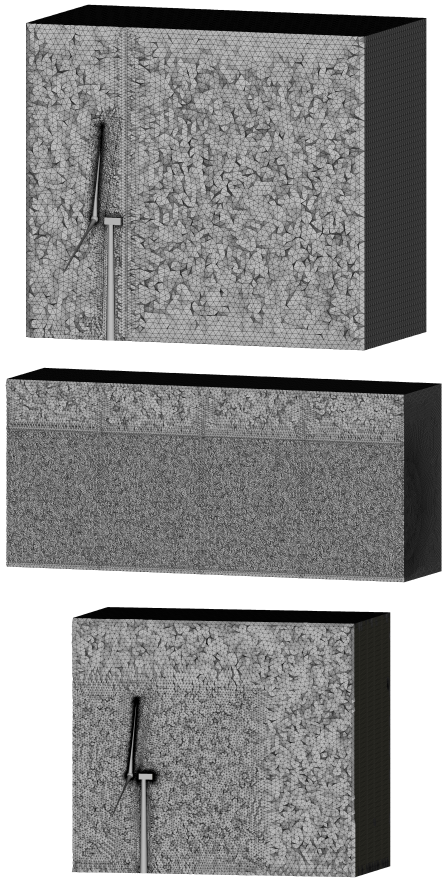

Fig. 28: Meshes used in the MDM wind-turbine aerodynamics and FSI simulations. *Top-to-bottom*: *Turbine 1*, *Box*, *Turbine 2*.

Figure 30 shows the vorticity isosurfaces. Rotor-tip vortices of the upstream turbine maintain a helical pattern for a distance of about one rotor diameter. They later break up, and eventually merge with vortices shed from the root and tower to form larger structures at a distance between two and three rotor

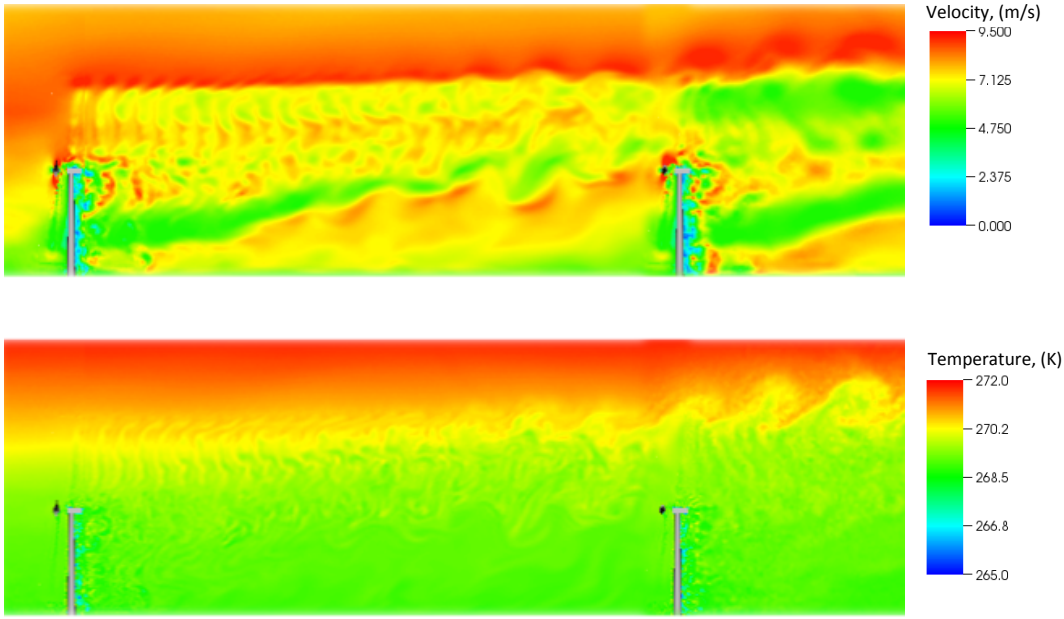

Fig. 29: 2D slice of the air speed (*top*) and temperature (*bottom*).

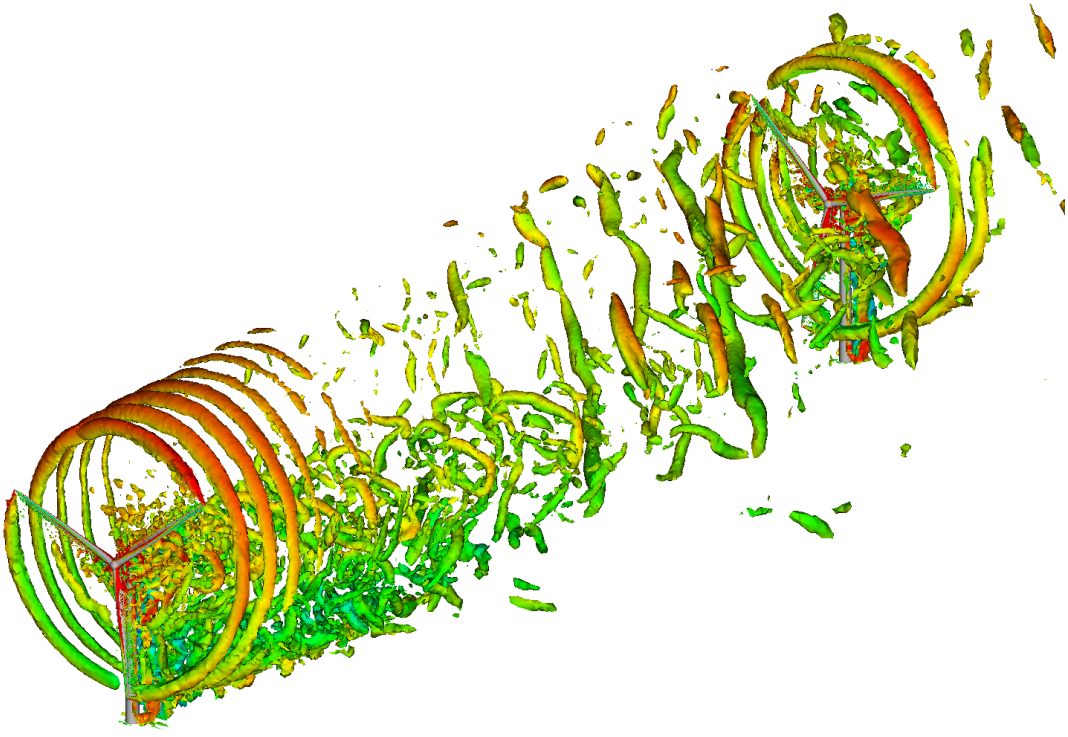

Fig. 30: 3D view of the vorticity isosurfaces colored by the air speed.

diameters (see Figure 30). These larger flow structures impact the downstream-turbine rotor and tower, and break up together with the rotor-tip vortices. The helical pattern of the rotor-tip vortices for the downstream turbine is only maintained for a short distance behind the rotor. This enhanced turbulent mixing gives a faster growth of the shear layer behind the downstream turbine.

Remark 2. *When simulating ABL flows, the computational domain should be large enough to account for the wake drift due to side wind and Coriolis force. Figure 31 shows the front view of the vorticity isosurfaces, where the wake drift is clearly seen. While in the present simulations wake drift is not as significant, for stronger side winds the computational domain needs to have a larger spanwise dimension.*

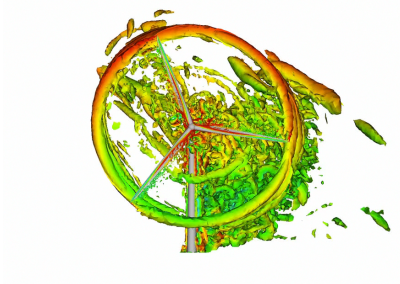

Fig. 31: Front view of the vorticity isosurfaces colored by the air speed.

Figure 32 shows the air speed, averaged over six rotor revolutions, at different locations along the centerline as a function of the vertical coordinate. Air speed profile at the inlet corresponds to that imposed from the LES simulation. A short distance past *Turbine 1* the profile appears distorted, and slowly begins to recover with increasing distance from the upstream turbine. By the location of *Turbine 2* the profile begins to recover up to the hub height and above the upper-blade tip. However, qualitative differences w.r.t. the inflow profile, e.g., less near-ground shear and a higher shear above the top of the upper rotor, may be observed. In between the hub-height and upper-blade-tip locations, one can clearly see the velocity deficit, which is on the order of 1–2 m/s. This velocity deficit leads to the power-production drop, as discussed in the next section.

14.3. FSI simulation

In this section we present FSI simulations of the same MDM set-up. The wind-turbine geometry, materials, and mesh, which is comprised of 13,273 quadratic NURBS shell elements, are taken from [41]. Figure 33 shows the aerodynamic torque acting on each blade of the upstream-turbine rotor, and compares the pure aerodynamics (labeled "CFD") and FSI results. The FSI simulation curves exhibit low frequency modes coming from the blade flapwise bending motions, as well as high-frequency modes coming from the blade axial torsion motions. These modes are obviously not present in the CFD curves, which underscore the importance of including FSI in the wind-turbine modeling, especially if one is interested in predicting the remaining useful fatigue life of wind-turbine structural components (see, e.g., [14]).

Figure 34 shows a comparison of the aerodynamic torque acting on the upstream and downstream turbines. The results confirm power losses for the downstream turbine of 10–15 % relative to the upstream turbine, which are due to the velocity deficit in the upstream-turbine wake. Also note that the amplitude of high-frequency oscillations due to the blade torsional motions is a little higher for the downstream turbine, which is due to higher turbulence intensity in the upstream-turbine wake than in the free stream. The nominal aerodynamic torque from the NREL baseline design for a uniform wind speed of 8 m/s [167] is also plotted for comparison to underscore the importance of including realistic boundary-layer flow in the aerodynamics and FSI modeling of wind turbines at full scale.

15. Concluding remarks

We have described how, with the VMS methods we developed in recent years, we are addressing the challenges faced in computational flow

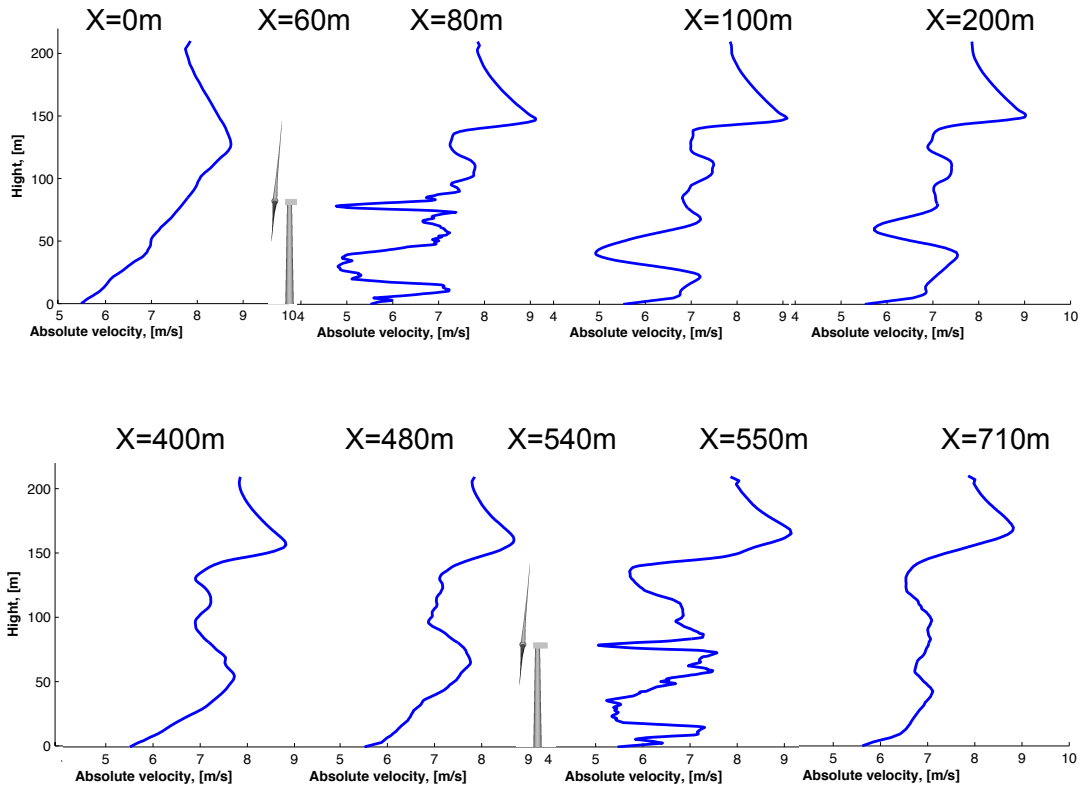

Fig. 32: Air speed averaged over six rotor revolutions and plotted at different locations along the centerline as a function of the vertical coordinate.

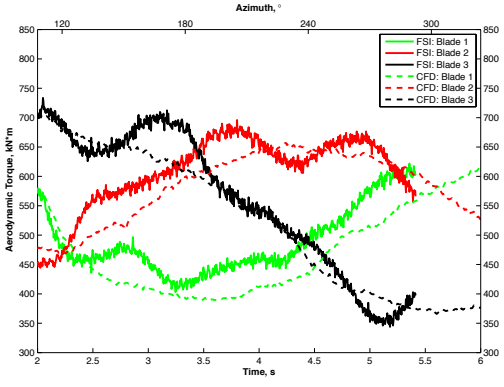

Fig. 33: Time history of the aerodynamic torque for each blade of the upstream turbine. Comparison of pure aerodynamics (labeled "CFD") and FSI simulation results. See Figure 25 for the blade numbering.

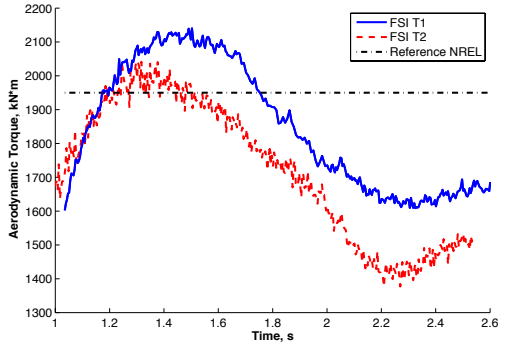

Fig. 34: Time history of the aerodynamic torque from FSI simulations of the upstream (T1) and downstream (T2) turbines. Aerodynamic torque for uniform wind speed of 8 m/s from [167] is shown for comparison.

analysis in aerospace, energy and transportation technologies. We have described how we are bringing solution in computationally challenging problems such as aerodynamics of parachutes, thermo-fluid analysis of ground vehicles and tires, and wind turbines operating in turbulent ABL flows. The computational challenges include complex geometries, MBI, FSI, turbulent flows, rotational flows, and large problem sizes. Our core computational methods in addressing the challenges are the RBVMS, ALE-VMS and ST-VMS. The special methods used in combination with the core methods include the ALE-SI, ST-SI, YZβ DC, ST-IGA, ST-SI-IGA, ST-C data compression, and MDM. We described the core and special methods. We presented, as examples of challenging computations performed with these methods, aerodynamic analysis of a ram-air parachute, thermo-fluid analysis of a freight truck and its rear set of tires, and aerodynamic and FSI analysis of two back-to-back wind turbines operating in thermally stratified ABL flow. The examples demonstrate the power and scope of the core and special methods in computational flow analysis in aerospace, energy and transportation technologies.

Acknowledgement

This work was supported (first author) in part by Grant-in-Aid for Challenging Exploratory Research 16K13779 from Japan Society for the Promotion of Science; Grant-in-Aid for Scientific Research (S) 26220002 from the Ministry of Education, Culture, Sports, Science and Technology of Japan (MEXT); Council for Science, Technology and Innovation (CSTI), Cross-Ministerial Strategic Innovation Promotion Program (SIP), "Innovative Combustion Technology" (Funding agency: JST); and Rice–Waseda research agreement. The mathematical model and computational method parts of the work were also supported (third author) in part by ARO Grant W911NF-17-1-0046, ARO DURIP Grant W911NF-18-1-0234, and Top Global University Project of Waseda University. The second author was partially supported by NSF Grant 1854436, and the fourth author was partially supported by NSERC Discovery Grant RGPIN-2017-03781.

References

[1] Takizawa, K., & Tezduyar, T. E. (2012). Computational Methods for Parachute Fluid–Structure Interactions. Archives of Computational Methods in Engineering, 19, 125–169.

[2] Takizawa, K., Montes, D., Fritze, M., McIntyre, S., Boben, J., & Tezduyar, T. E. (2013). Methods for FSI modeling of spacecraft parachute dynamics and cover separation. Mathematical Models and Methods in Applied Sciences, 23, 307–338.

[3] Takizawa, K., Tezduyar, T. E., & Kolesar, R. (2015). FSI Modeling of the Orion Spacecraft Drogue Parachutes. Computational Mechanics, 55, 1167–1179.

[4] Takizawa, K., Tezduyar, T. E., & Terahara, T. (2016). Ram-Air Parachute Structural and Fluid Mechanics Computations with the Space–Time Isogeometric Analysis (ST-IGA). Computers & Fluids, 141, 191–200.

[5] Takizawa, K., Tezduyar, T. E., & Kanai, T. (2017). Porosity models and computational methods for compressible-flow aerodynamics of parachutes with geometric porosity. Mathematical Models and Methods in Applied Sciences, 27, 771–806.

[6] Takizawa, K., Tezduyar, T. E., & Kuraishi, T. (2015). Multiscale ST Methods for Thermo-Fluid Analysis of a Ground Vehicle and its Tires. Mathematical Models and Methods in Applied Sciences, 25, 2227–2255.

[7] Kuraishi, T., Takizawa, K., & Tezduyar, T. E. (2019). Tire Aerodynamics with Actual Tire Geometry, Road Contact and Tire Deformation. Computational Mechanics, 63, 1165–1185.

[8] Takizawa, K., Tezduyar, T. E., Kuraishi, T., Tabata, S., & Takagi, H. (2016). Computational thermo-fluid analysis of a disk brake. Computational Mechanics, 57, 965–977.

[9] Otoguro, Y., Takizawa, K., Tezduyar, T. E., Nagaoka, K., & Mei, S. (2019). Turbocharger turbine and exhaust manifold flow computation with the Space–Time Variational Multiscale Method and Isogeometric Analysis. Computers & Fluids, 179, 764–776.

[10] Bazilevs, Y., Korobenko, A., Deng, X., & Yan, J. (2015). Novel structural modeling and mesh moving techniques for advanced FSI simulation of wind turbines. International Journal for Numerical Methods in Engineering, 102, 766–783.

[11] Bazilevs, Y., Korobenko, A., Deng, X., Yan, J., Kinzel, M., & Dabiri, J. O. (2014). FSI modeling of vertical-axis wind turbines. Journal of Applied Mechanics, 81, 081006.

[12] Yan, J., Korobenko, A., Deng, X., & Bazilevs, Y. (2016). Computational free-surface fluid–structure interaction with application to floating offshore wind turbines. Computers and Fluids, 141, 155–174.

[13] Bazilevs, Y., Korobenko, A., Yan, J., Pal, A., Gohari, S. M. I., & Sarkar, S. (2015). ALE–VMS Formulation for Stratified Turbulent Incompressible Flows with Applications. Mathematical Models and Methods in Applied Sciences, 25, 2349–2375.

[14] Bazilevs, Y., Korobenko, A., Deng, X., & Yan, J. (2016). FSI modeling for fatigue-damage prediction in full-scale wind-turbine blades. Journal of Applied Mechanics, 83(6), 061010.

[15] Hughes, T. J. R. (1995). Multiscale Phenomena: Green's Functions, The Dirichlet-to-Neumann Formulation, Subgrid Scale Models, Bubbles, and the Origins of Stabilized Methods. Computer Methods in Applied Mechanics and Engineering, 127, 387–401.

[16] Hughes, T. J. R., Oberai, A. A., & Mazzei, L. (2001). Large Eddy Simulation of Turbulent Channel Flows by the Variational Multiscale Method. Physics of Fluids, 13, 1784–1799.

[17] Bazilevs, Y., Calo, V. M., Cottrell, J. A., Hughes, T. J. R., Reali, A., & Scovazzi, G. (2007). Variational multiscale residual-based turbulence modeling for large eddy simulation of incompressible flows. Computer Methods in Applied Mechanics and Engineering, 197, 173–201.

[18] Bazilevs, Y., & Akkerman, I. (2010). Large eddy simulation of turbulent Taylor–Couette flow using isogeometric analysis and the residual–based variational multiscale method. Journal of Computational Physics, 229, 3402–3414.

[19] Bazilevs, Y., Calo, V. M., Hughes, T. J. R., & Zhang, Y. (2008). Isogeometric fluid–structure interaction: theory, algorithms, and computations. Computational Mechanics, 43, 3–37.

[20] Takizawa, K., Bazilevs, Y., & Tezduyar, T. E. (2012). Space–Time and ALE-VMS Techniques for Patient-Specific Cardiovascular Fluid–Structure Interaction Modeling. Archives of Computational Methods in Engineering, 19, 171–225.

[21] Bazilevs, Y., Hsu, M.-C., Takizawa, K., & Tezduyar, T. E. (2012). ALE-VMS and ST-VMS Methods for Computer Modeling of Wind-Turbine Rotor Aerodynamics and Fluid–Structure Interaction. Mathematical Models and Methods in Applied Sciences, 22(supp02), 1230002.

[22] Bazilevs, Y., Takizawa, K., & Tezduyar, T. E. (February 2013). Computational Fluid–Structure Interaction: Methods and Applications. Wiley.

[23] Bazilevs, Y., Takizawa, K., & Tezduyar, T. E. (2013). Challenges and Directions in Computational Fluid–Structure Interaction. Mathematical Models and Methods in Applied Sciences, 23, 215–221.

[24] Bazilevs, Y., Takizawa, K., & Tezduyar, T. E. (2015). New Directions and Challenging Computations in Fluid Dynamics Modeling with Stabilized and Multiscale Methods. Mathematical Models and Methods in Applied Sciences, 25, 2217–2226.

[25] Bazilevs, Y., Takizawa, K., & Tezduyar, T. E. (2019). Computational Analysis Methods for Complex Unsteady Flow Problems. Mathematical Models and Methods in Applied Sciences, 29, 825–838.

[26] Takizawa, K., & Tezduyar, T. E. (2011). Multiscale Space–Time Fluid–Structure Interaction Techniques. Computational Mechanics, 48, 247–267.

[27] Takizawa, K., & Tezduyar, T. E. (2012). Space–Time Fluid–Structure Interaction Methods. Mathematical Models and Methods in Applied Sciences, 22(supp02), 1230001.

[28] Takizawa, K., Tezduyar, T. E., Mochizuki, H., Hattori, H., Mei, S., Pan, L., & Montel, K. (2015). Space–time VMS method for flow computations with slip interfaces (ST-SI). Mathematical Models and Methods in Applied Sciences, 25, 2377–2406.

[29] Takizawa, K., Henicke, B., Puntel, A., Spielman, T., & Tezduyar, T. E. (2012). Space–time computational techniques for the aerodynamics of flapping wings. Journal of Applied Mechanics, 79, 010903.

[30] Takizawa, K., Tezduyar, T. E., Otoguro, Y., Terahara, T., Kuraishi, T., & Hattori, H. (2017). Turbocharger Flow Computations with the Space–Time Isogeometric Analysis (ST-IGA). Computers & Fluids, 142, 15–20.

[31] Osawa, Y., Kalro, V., & Tezduyar, T. (1999). Multi-Domain Parallel Computation of Wake Flows. Computer Methods in Applied Mechanics and Engineering, 174, 371–391.

[32] Takizawa, K., & Tezduyar, T. E. (2014). Space–time computation techniques with continuous representation in time (ST-C). Computational Mechanics, 53, 91–99.

[33] Bazilevs, Y., & Hughes, T. J. R. (2007). Weak imposition of Dirichlet boundary conditions in fluid mechanics. Computers and Fluids, 36, 12–26.

[34] Bazilevs, Y., Michler, C., Calo, V. M., & Hughes, T. J. R. (2010). Isogeometric variational multiscale modeling of wall-bounded turbulent flows with weakly enforced boundary conditions on unstretched meshes. Computer Methods in Applied Mechanics and Engineering, 199, 780–790.

[35] Hsu, M.-C., Akkerman, I., & Bazilevs, Y. (2012). Wind turbine aerodynamics using ALE-VMS: Validation and role of weakly enforced boundary conditions. Computational Mechanics, 50, 499–511.

[36] Bazilevs, Y., & Hughes, T. J. R. (2008). NURBS-based isogeometric analysis for the computation of flows about rotating components. Computational Mechanics, 43, 143–150.

[37] Hsu, M.-C., & Bazilevs, Y. (2012). Fluid–structure interaction modeling of wind turbines: simulating the full machine. Computational Mechanics, 50, 821–833.

[38] Takizawa, K., Bazilevs, Y., Tezduyar, T. E., & Korobenko, A. (2020). Variational Multiscale Flow Analysis in Aerospace, Energy and Transportation Technologies. In: Grama, A., & Sameh, A. (Eds.), Parallel Algorithms in Computational Science and Engineering, Modeling and Simulation in Science, Engineering and Technology. Springer.

[39] Kalro, V., & Tezduyar, T. E. (2000). A Parallel 3D Computational Method for Fluid–Structure Interactions in Parachute Systems. Computer Methods in Applied Mechanics and Engineering, 190, 321–332.

[40] Kalro, V., Aliabadi, S., Garrard, W., Tezduyar, T., Mittal, S., & Stein, K.

(1997). Parallel Finite Element Simulation of Large Ram-Air Parachutes. International Journal for Numerical Methods in Fluids, 24, 1353–1369.

[41] Korobenko, A., Yan, J., Gohari, S. M. I., Sarkar, S., & Bazilevs, Y. (2017). FSI simulation of two back-to-back wind turbines in atmospheric boundary layer flow. Computers & Fluids, 158, 167–175.

[42] Tezduyar, T. E. (1992). Stabilized Finite Element Formulations for Incompressible Flow Computations. Advances in Applied Mechanics, 28, 1–44.

[43] Tezduyar, T. E. (2003). Computation of Moving Boundaries and Interfaces and Stabilization Parameters. International Journal for Numerical Methods in Fluids, 43, 555–575.

[44] Tezduyar, T. E., & Sathe, S. (2007). Modeling of Fluid–Structure Interactions with the Space–Time Finite Elements: Solution Techniques. International Journal for Numerical Methods in Fluids, 54, 855–900.

[45] Brooks, A. N., & Hughes, T. J. R. (1982). Streamline Upwind/Petrov-Galerkin Formulations for Convection Dominated Flows with Particular Emphasis on the Incompressible Navier-Stokes Equations. Computer Methods in Applied Mechanics and Engineering, 32, 199–259.

[46] Tezduyar, T. E., & Takizawa, K. (2019). Space–time computations in practical engineering applications: A summary of the 25-year history. Computational Mechanics, 63, 747–753.

[47] Takizawa, K., Fritze, M., Montes, D., Spielman, T., & Tezduyar, T. E. (2012). Fluid–structure interaction modeling of ringsail parachutes with disreefing and modified geometric porosity. Computational Mechanics, 50, 835–854.

[48] Takizawa, K., Tezduyar, T. E., Boben, J., Kostov, N., Boswell, C., & Buscher, A. (2013). Fluid–structure interaction modeling of clusters of spacecraft parachutes with modified geometric porosity. Computational Mechanics, 52, 1351–1364.

[49] Takizawa, K., Tezduyar, T. E., Boswell, C., Tsutsui, Y., & Montel, K. (2015). Special Methods for Aerodynamic-Moment Calculations from Parachute FSI Modeling. Computational Mechanics, 55, 1059–1069.

[50] Takizawa, K., Tezduyar, T. E., Boswell, C., Kolesar, R., & Montel, K. (2014). FSI Modeling of the Reefed Stages and Disreefing of the Orion Spacecraft Parachutes. Computational Mechanics, 54, 1203–1220.

[51] Takizawa, K., Tezduyar, T. E., Kolesar, R., Boswell, C., Kanai, T., & Montel, K. (2014). Multiscale Methods for Gore Curvature Calculations from FSI Modeling of Spacecraft Parachutes. Computational Mechanics, 54, 1461–1476.

[52] Bazilevs, Y., Hsu, M.-C., Akkerman, I., Wright, S., Takizawa, K., Henicke, B., Spielman, T., & Tezduyar, T. E. (2011). 3D Simulation of Wind Turbine Rotors at Full Scale. Part I: Geometry Modeling and Aerodynamics. International Journal for Numerical Methods in Fluids, 65, 207–235.

[53] Takizawa, K., Henicke, B., Tezduyar, T. E., Hsu, M.-C., & Bazilevs, Y. (2011). Stabilized Space–Time Computation of Wind-Turbine Rotor Aerodynamics. Computational Mechanics, 48, 333–344.

[54] Takizawa, K., Henicke, B., Montes, D., Tezduyar, T. E., Hsu, M.-C., & Bazilevs, Y. (2011). Numerical-Performance Studies for the Stabilized Space–Time Computation of Wind-Turbine Rotor Aerodynamics. Computational Mechanics, 48, 647–657.

[55] Takizawa, K., Tezduyar, T. E., McIntyre, S., Kostov, N., Kolesar, R., & Habluetzel, C. (2014). Space–time VMS computation of wind-turbine rotor and tower aerodynamics. Computational Mechanics, 53, 1–15.

[56] Takizawa, K., Bazilevs, Y., Tezduyar, T. E., Hsu, M.-C., Øiseth, O., Mathisen, K. M., Kostov, N., & McIntyre, S. (2014). Engineering Analysis and Design with ALE-VMS and Space–Time Methods. Archives of Computational Methods in Engineering, 21, 481–508.

[57] Takizawa, K. (2014). Computational Engineering Analysis with the New-Generation Space–Time Methods. Computational Mechanics, 54, 193–211.

[58] Bazilevs, Y., Takizawa, K., Tezduyar, T. E., Hsu, M.-C., Kostov, N., & McIntyre, S. (2014). Aerodynamic and FSI Analysis of Wind Turbines with the ALE-VMS and ST-VMS Methods. Archives of Computational Methods in Engineering, 21, 359–398.

[59] Korobenko, A., Bazilevs, Y., Takizawa, K., & Tezduyar, T. E. (2018). Recent Advances in ALE-VMS and ST-VMS Computational Aerodynamic and FSI Analysis of Wind Turbines. In: Tezduyar, T. E. (Ed.), Frontiers in Computational Fluid–Structure Interaction and Flow Simulation: Research from Lead Investigators under Forty – 2018, Modeling and Simulation in Science, Engineering and Technology. Springer, 253–336.

[60] Korobenko, A., Bazilevs, Y., Takizawa, K., & Tezduyar, T. E. (2019). Computer modeling of wind turbines: 1. ALE-VMS and ST-VMS aerodynamic and FSI analysis. Archives of Computational Methods in Engineering, 26, 1059–1099.

[61] Takizawa, K., Henicke, B., Puntel, A., Kostov, N., & Tezduyar, T. E. (2012). Space–Time Techniques for Computational Aerodynamics Modeling of Flapping Wings of an Actual Locust. Computational Mechanics, 50, 743–760.

[62] Takizawa, K., Henicke, B., Puntel, A., Kostov, N., & Tezduyar, T. E. (2013). Computer Modeling Techniques for Flapping-Wing Aerodynamics of a Locust. Computers & Fluids, 85, 125–134.

[63] Takizawa, K., Kostov, N., Puntel, A., Henicke, B., & Tezduyar, T. E. (2012). Space–time computational analysis of bio-inspired flapping-wing aerodynamics of a micro aerial vehicle. Computational Mechanics, 50, 761–778.

[64] Takizawa, K., Tezduyar, T. E., & Kostov, N. (2014). Sequentially-coupled space–time FSI analysis of bio-inspired flapping-wing aerodynamics of an MAV. Computational Mechanics, 54, 213–233.

[65] Takizawa, K., Tezduyar, T. E., Buscher, A., & Asada, S. (2014). Space–Time Interface-Tracking with Topology Change (ST-TC). Computational Mechanics, 54, 955–971.

[66] Takizawa, K., Tezduyar, T. E., & Buscher, A. (2015). Space–Time Computational Analysis of MAV Flapping-Wing Aerodynamics with Wing Clapping. Computational Mechanics, 55, 1131–1141.

[67] Takizawa, K., Bazilevs, Y., Tezduyar, T. E., Long, C. C., Marsden, A. L., & Schjodt, K. (2014). ST and ALE-VMS Methods for Patient-Specific Cardiovascular Fluid Mechanics Modeling. Mathematical Models and Methods in Applied Sciences, 24, 2437–2486.

[68] Takizawa, K., Schjodt, K., Puntel, A., Kostov, N., & Tezduyar, T. E. (2012). Patient-specific computer modeling of blood flow in cerebral arteries with aneurysm and stent. Computational Mechanics, 50, 675–686.

[69] Takizawa, K., Schjodt, K., Puntel, A., Kostov, N., & Tezduyar, T. E. (2013). Patient-Specific Computational Analysis of the Influence of a Stent on the Unsteady Flow in Cerebral Aneurysms. Computational Mechanics, 51, 1061–1073.

[70] Suito, H., Takizawa, K., Huynh, V. Q. H., Sze, D., & Ueda, T. (2014). FSI analysis of the blood flow and geometrical characteristics in the thoracic aorta. Computational Mechanics, 54, 1035–1045.

[71] Suito, H., Takizawa, K., Huynh, V. Q. H., Sze, D., Ueda, T., & Tezduyar, T. E. (2016). A geometrical-characteristics study in patient-specific FSI analysis of blood flow in the thoracic aorta. In: Bazilevs, Y., & Takizawa, K. (Eds.), Advances in Computational Fluid–Structure Interaction and Flow Simulation: New Methods and Challenging Computations, Modeling and Simulation in Science, Engineering and Technology. Springer, 379–386.

[72] Takizawa, K., Tezduyar, T. E., Uchikawa, H., Terahara, T., Sasaki, T., Shiozaki, K., Yoshida, A., Komiya, K., & Inoue, G. (2018). Aorta Flow Analysis and Heart Valve Flow and Structure Analysis. In: Tezduyar, T. E. (Ed.), Frontiers in Computational Fluid–Structure Interaction and Flow Simulation: Research from Lead Investigators under Forty – 2018, Modeling and Simulation in Science, Engineering and Technology. Springer, 29–89.

[73] Takizawa, K., Tezduyar, T. E., Uchikawa, H., Terahara, T., Sasaki, T., & Yoshida, A. (2019). Mesh refinement influence and cardiac-cycle flow periodicity in aorta flow analysis with isogeometric discretization. Computers & Fluids, 179, 790–798.

[74] Takizawa, K., Bazilevs, Y., Tezduyar, T. E., & Hsu, M.-C. (2019). Computational Cardiovascular Flow Analysis with the Variational Multiscale Methods. Journal of Advanced Engineering and Computation, 3, 366–405.

[75] Takizawa, K., Tezduyar, T. E., Buscher, A., & Asada, S. (2014). Space–Time Fluid Mechanics Computation of Heart Valve Models. Computational Mechanics, 54, 973–986.

[76] Takizawa, K., & Tezduyar, T. E. (2016). New directions in space–time computational methods. In: Bazilevs, Y., & Takizawa, K. (Eds.), Advances in Computational Fluid–Structure Interaction and Flow Simulation: New Methods and Challenging Computations, Modeling and Simulation in Science, Engineering and Technology. Springer, 159–178.

[77] Takizawa, K., Tezduyar, T. E., Terahara, T., & Sasaki, T. (2018). Heart valve flow computation with the Space–Time Slip Interface Topology Change (ST-SI-TC) method and Isogeometric Analysis (IGA). In: Wriggers, P., & Lenarz, T. (Eds.), Biomedical Technology: Modeling, Experiments and Simulation, Lecture Notes in Applied and Computational Mechanics. Springer, 77–99.

[78] Takizawa, K., Tezduyar, T. E., Terahara, T., & Sasaki, T. (2017). Heart valve flow computation with the integrated Space–Time VMS, Slip Interface, Topology Change and Isogeometric Discretization methods. Computers & Fluids, 158, 176–188.

[79] Terahara, T., Takizawa, K., Tezduyar, T. E., Bazilevs, Y., & Hsu, M.-C. (2020). Heart Valve Isogeometric Sequentially-Coupled FSI Analysis with the Space–Time Topology Change Method. *Computational Mechanics*, 65, 1167–1187, DOI: 10.1007/s00466-019-01813-0.

[80] Terahara, T., Takizawa, K., Tezduyar, T. E., Tsushima, A., & Shiozaki, K. (2020). Ventricle-valve-aorta flow analysis with the Space–Time Isogeometric Discretization and Topology Change. *Computational Mechanics*, 65, 1343–1363, DOI: 10.1007/s00466-020-01822-4.

[81] Yu, Y., Zhang, Y. J., Takizawa, K., Tezduyar, T. E., & Sasaki, T. (2020). Anatomically Realistic Lumen Motion Representation in Patient-Specific Space–Time Isogeometric Flow Analysis of Coronary Arteries with Time-Dependent Medical-Image Data. Computational Mechanics, 65, 395–404.

[82] Takizawa, K., Montes, D., McIntyre, S., & Tezduyar, T. E. (2013). Space–Time VMS Methods for Modeling of Incompressible Flows at High Reynolds Numbers. Mathematical Models and Methods in Applied Sciences, 23, 223–248.

[83] Takizawa, K., Tezduyar, T. E., & Hattori, H. (2017). Computational Analysis of Flow-Driven String Dynamics in Turbomachinery. Computers & Fluids, 142, 109–117.

[84] Komiya, K., Kanai, T., Otoguro, Y., Kaneko, M., Hirota, K., Zhang, Y., Takizawa, K., Tezduyar, T. E., Nohmi, M., Tsuneda, T., Kawai, M., & Isono, M. (2019). Computational analysis of flow-driven string dynamics in a pump and residence time calculation. IOP conference series earth and environmental science, 240, 062014.

[85] Kanai, T., Takizawa, K., Tezduyar, T. E., Komiya, K., Kaneko, M., Hirota, K., Nohmi, M., Tsuneda, T., Kawai, M., & Isono, M. (2019). Methods for Computation of Flow-Driven String Dynamics in a Pump and Residence Time. Mathematical Models and Methods in Applied Sciences, 29, 839–870.

[86] Otoguro, Y., Takizawa, K., & Tezduyar, T. E. (2017). Space–time VMS computational flow analysis with isogeometric discretization and a general-purpose NURBS mesh generation method. Computers & Fluids, 158, 189–200.

[87] Otoguro, Y., Takizawa, K., & Tezduyar, T. E. (2018). A General-Purpose NURBS Mesh Generation Method for Complex Geometries. In: Tezduyar, T. E. (Ed.), Frontiers in Computational Fluid–Structure Interaction and Flow Simulation: Research from Lead Investigators under Forty – 2018, Modeling and Simulation in Science, Engineering and Technology. Springer, 399–434.

[88] Otoguro, Y., Takizawa, K., Tezduyar, T. E., Nagaoka, K., Avsar, R., & Zhang, Y. (2019). Space–Time VMS Flow Analysis of a Turbocharger Turbine with Isogeometric Discretization: Computations with Time-Dependent and Steady-Inflow Representations of the Intake/Exhaust Cycle. Computational Mechanics, 64, 1403–1419.

[89] Takizawa, K., Tezduyar, T. E., Asada, S., & Kuraishi, T. (2016). Space–Time Method for Flow Computations with Slip Interfaces and Topology Changes (ST-SI-TC). Computers & Fluids, 141, 124–134.

[90] Kuraishi, T., Takizawa, K., & Tezduyar, T. E. (2018). Space–Time Computational Analysis of Tire Aerodynamics with Actual Geometry, Road Contact and Tire Deformation. In: Tezduyar, T. E. (Ed.), Frontiers in Computational Fluid–Structure Interaction and Flow Simulation: Research from Lead Investigators under Forty – 2018, Modeling and Simulation in Science, Engineering and Technology. Springer, 337–376.

[91] Kuraishi, T., Takizawa, K., & Tezduyar, T. E. (2019). Space–Time Computational Analysis of Tire Aerodynamics with Actual Geometry, Road Contact, Tire Deformation, Road Roughness and Fluid Film. Computational Mechanics, 64, 1699–1718.

[92] Kuraishi, T., Takizawa, K., & Tezduyar, T. E. (2019). Space–Time Isogeometric Flow Analysis with Built-in Reynolds-Equation Limit. Mathematical Models and Methods in Applied Sciences, 29, 871–904.

[93] Kanai, T., Takizawa, K., Tezduyar, T. E., Tanaka, T., & Hartmann, A. (2019). Compressible-Flow Geometric-Porosity Modeling and Spacecraft Parachute Computation with Isogeometric Discretization. Computational Mechanics, 63, 301–321.

[94] Hughes, T. J. R., Liu, W. K., & Zimmermann, T. K. (1981). Lagrangian–Eulerian finite element formulation for incompressible viscous flows. Computer Methods in Applied Mechanics and Engineering, 29, 329–349.

[95] Bazilevs, Y., Hsu, M.-C., Kiendl, J., Wüchner, R., & Bletzinger, K.-U. (2011). 3D simulation of wind turbine rotors at full scale. Part II: Fluid–structure interaction modeling with composite blades. International Journal for Numerical Methods in Fluids, 65, 236–253.

[96] Hsu, M.-C., Akkerman, I., & Bazilevs, Y. (2011). High-performance computing of

wind turbine aerodynamics using isogeometric analysis. Computers and Fluids, 49, 93–100.

[97] Bazilevs, Y., Hsu, M.-C., & Scott, M. A. (2012). Isogeometric Fluid–Structure Interaction Analysis with Emphasis on Non-Matching Discretizations, and with Application to Wind Turbines. Computer Methods in Applied Mechanics and Engineering, 249-252, 28–41.

[98] Hsu, M.-C., Akkerman, I., & Bazilevs, Y. (2014). Finite element simulation of wind turbine aerodynamics: Validation study using NREL Phase VI experiment. Wind Energy, 17, 461–481.

[99] Korobenko, A., Hsu, M.-C., Akkerman, I., Tippmann, J., & Bazilevs, Y. (2013). Structural mechanics modeling and FSI simulation of wind turbines. Mathematical Models and Methods in Applied Sciences, 23, 249–272.

[100] Korobenko, A., Hsu, M.-C., Akkerman, I., & Bazilevs, Y. (2013). Aerodynamic simulation of vertical-axis wind turbines. Journal of Applied Mechanics, 81, 021011.

[101] Bazilevs, Y., Calo, V. M., Zhang, Y., & Hughes, T. J. R. (2006). Isogeometric fluid–structure interaction analysis with applications to arterial blood flow. Computational Mechanics, 38, 310–322.

[102] Bazilevs, Y., Gohean, J. R., Hughes, T. J. R., Moser, R. D., & Zhang, Y. (2009). Patient-specific isogeometric fluid–structure interaction analysis of thoracic aortic blood flow due to implantation of the Jarvik 2000 left ventricular assist device. Computer Methods in Applied Mechanics and Engineering, 198, 3534–3550.

[103] Bazilevs, Y., Hsu, M.-C., Benson, D., Sankaran, S., & Marsden, A. (2009). Computational Fluid–Structure Interaction: Methods and Application to a Total Cavopulmonary Connection. Computational Mechanics, 45, 77–89.

[104] Bazilevs, Y., Hsu, M.-C., Zhang, Y., Wang, W., Liang, X., Kvamsdal, T., Brekken, R., & Isaksen, J. (2010). A Fully-Coupled Fluid–Structure Interaction Simulation of Cerebral Aneurysms. Computational Mechanics, 46, 3–16.

[105] Bazilevs, Y., Hsu, M.-C., Zhang, Y., Wang, W., Kvamsdal, T., Hentschel, S., & Isaksen, J. (2010). Computational Fluid–Structure Interaction: Methods and Application to Cerebral Aneurysms. Biomechanics and Modeling in Mechanobiology, 9, 481–498.

[106] Hsu, M.-C., & Bazilevs, Y. (2011). Blood vessel tissue prestress modeling for vascular fluid–structure interaction simulations. Finite Elements in Analysis and Design, 47, 593–599.

[107] Long, C. C., Marsden, A. L., & Bazilevs, Y. (2013). Fluid–structure interaction simulation of pulsatile ventricular assist devices. Computational Mechanics, 52, 971–981.

[108] Long, C. C., Esmaily-Moghadam, M., Marsden, A. L., & Bazilevs, Y. (2014). Computation of residence time in the simulation of pulsatile ventricular assist devices. Computational Mechanics, 54, 911–919.

[109] Long, C. C., Marsden, A. L., & Bazilevs, Y. (2014). Shape optimization of pulsatile ventricular assist devices using FSI to minimize thrombotic risk. Computational Mechanics, 54, 921–932.

[110] Hsu, M.-C., Kamensky, D., Bazilevs, Y., Sacks, M. S., & Hughes, T. J. R. (2014). Fluid–structure interaction analysis of bioprosthetic heart valves: significance of arterial wall deformation. Computational Mechanics, 54, 1055–1071.

[111] Hsu, M.-C., Kamensky, D., Xu, F., Kiendl, J., Wang, C., Wu, M. C. H., Mineroff, J., Reali, A., Bazilevs, Y., & Sacks, M. S. (2015). Dynamic and fluid–structure interaction simulations of bioprosthetic heart valves using parametric design with T-splines and Fung-type material models. Computational Mechanics, 55, 1211–1225.

[112] Kamensky, D., Hsu, M.-C., Schillinger, D., Evans, J. A., Aggarwal, A., Bazilevs, Y., Sacks, M. S., & Hughes, T. J. R. (2015). An immersogeometric variational framework for fluid-structure interaction: Application to bioprosthetic heart valves. Computer Methods in Applied Mechanics and Engineering, 284, 1005–1053.

[113] Akkerman, I., Bazilevs, Y., Benson, D. J., Farthing, M. W., & Kees, C. E. (2012). Free-Surface Flow and Fluid–Object Interaction Modeling with Emphasis on Ship Hydrodynamics. Journal of Applied Mechanics, 79, 010905.

[114] Akkerman, I., Dunaway, J., Kvandal, J., Spinks, J., & Bazilevs, Y. (2012). Toward free-surface modeling of planing vessels: simulation of the Fridsma hull using ALE-VMS. Computational Mechanics, 50, 719–727.

[115] Wang, C., Wu, M. C. H., Xu, F., Hsu, M.-C., & Bazilevs, Y. (2017). Modeling of a hydraulic arresting gear using fluid–structure interaction and isogeometric analysis. Computers and Fluids, 142, 3–14.

[116] Wu, M. C. H., Kamensky, D., Wang, C., Herrema, A. J., Xu, F., Pigazzini, M. S., Verma, A., Marsden, A. L., Bazilevs, Y., & Hsu, M.-C. (2017). Optimizing fluid–structure interaction systems with immersogeometric analysis and surrogate modeling: Application to a hydraulic arresting gear. Computer Methods in Applied Mechanics and Engineering, 316, 668–693.

[117] Yan, J., Deng, X., Korobenko, A., & Bazilevs, Y. (2017). Free-surface flow modeling and simulation of horizontal-axis tidal-stream turbines. Computers and Fluids, 158, 157–166.

[118] Castorrini, A., Corsini, A., Rispoli, F., Takizawa, K., & Tezduyar, T. E. (2019). A stabilized ALE method for computational fluid–structure interaction analysis of passive morphing in turbomachinery. Mathematical Models and Methods in Applied Sciences, 29, 967–994.

[119] Augier, B., Yan, J., Korobenko, A., Czarnowski, J., Ketterman, G., & Bazilevs, Y. (2015). Experimental and numerical FSI study of compliant hydrofoils. Computational Mechanics, 55, 1079–1090.

[120] Yan, J., Augier, B., Korobenko, A., Czarnowski, J., Ketterman, G., & Bazilevs, Y. (2016). FSI modeling of a propulsion system based on compliant hydrofoils in a tandem configuration. Computers and Fluids, 141, 201–211.

[121] Helgedagsrud, T. A., Bazilevs, Y., Mathisen, K. M., & Oiseth, O. A. Computational and experimental investigation of free vibration and flutter of bridge decks. Computational Mechanics. Published online.

[122] Helgedagsrud, T. A., Bazilevs, Y., Korobenko, A., Mathisen, K. M., & Oiseth, O. A. Using ALE-VMS to compute aerodynamic derivatives of bridge sections. Computers and Fluids. Published online.

[123] Helgedagsrud, T. A., Akkerman, I., Bazilevs, Y., Mathisen, K. M., & Oiseth, O. A. (2019). Isogeometric modeling and experimental investigation of moving-domain bridge aerodynamics. ASCE Journal of Engineering Mechanics, 145, 04019026.

[124] Kamensky, D., Evans, J. A., Hsu, M.-C., & Bazilevs, Y. (2017). Projection-based stabilization of interface Lagrange multipliers in immersogeometric fluid–thin structure interaction analysis, with application to heart valve modeling. Computers and Mathematics with Applications, 74, 2068–2088.

[125] Yu, Y., Kamensky, D., Hsu, M.-C., Lu, X. Y., Bazilevs, Y., & Hughes, T. J. R. (2018). Error estimates for projection-based dynamic augmented Lagrangian boundary condition enforcement, with application to fluid–structure interaction. Mathematical Models and Methods in Applied Science, 28, 2457–2509.

[126] Tezduyar, T. E., Takizawa, K., Moorman, C., Wright, S., & Christopher, J. (2010).

Space–Time Finite Element Computation of Complex Fluid–Structure Interactions. International Journal for Numerical Methods in Fluids, 64, 1201–1218.

[127] Yan, J., Korobenko, A., Tejada-Martinez, A. E., Golshan, R., & Bazilevs, Y. (2017). A new variational multiscale formulation for stratified incompressible turbulent flows. Computers & Fluids, 158, 150–156.

[128] van Opstal, T. M., Yan, J., Coley, C., Evans, J. A., Kvamsdal, T., & Bazilevs, Y. (2017). Isogeometric divergence-conforming variational multiscale formulation of incompressible turbulent flows. Computer Methods in Applied Mechanics and Engineering, 316, 859–879.

[129] Xu, F., Moutsanidis, G., Kamensky, D., Hsu, M.-C., Murugan, M., Ghoshal, A., & Bazilevs, Y. (2017). Compressible flows on moving domains: Stabilized methods, weakly enforced essential boundary conditions, sliding interfaces, and application to gas-turbine modeling. Computers & Fluids, 158, 201–220.

[130] Tezduyar, T. E., Aliabadi, S. K., Behr, M., & Mittal, S. (1994). Massively Parallel Finite Element Simulation of Compressible and Incompressible Flows. Computer Methods in Applied Mechanics and Engineering, 119, 157–177.

[131] Hsu, M.-C., Bazilevs, Y., Calo, V. M., Tezduyar, T. E., & Hughes, T. J. R. (2010). Improving Stability of Stabilized and Multiscale Formulations in Flow Simulations at Small Time Steps. Computer Methods in Applied Mechanics and Engineering, 199, 828–840.

[132] Takizawa, K., Tezduyar, T. E., & Otoguro, Y. (2018). Stabilization and discontinuity-capturing parameters for space–time flow computations with finite element and isogeometric discretizations. Computational Mechanics, 62, 1169–1186.

[133] Takizawa, K., Ueda, Y., & Tezduyar, T. E. (2019). A Node-Numbering-Invariant Directional Length Scale for Simplex Elements. Mathematical Models and Methods in Applied Sciences, 29, 2719–2753.

[134] Otoguro, Y., Takizawa, K., & Tezduyar, T. E. (2020). Element Length Calculation in B-Spline meshes for Complex Geometries. *Computational Mechanics*, 65, 1085–1103, DOI: 10.1007/s00466-019-01809-w.

[135] Corsini, A., Menichini, C., Rispoli, F., Santoriello, A., & Tezduyar, T. E. (2009). A Multiscale Finite Element Formulation with Discontinuity Capturing for Turbulence Models with Dominant Reactionlike Terms. Journal of Applied Mechanics, 76, 021211.

[136] Rispoli, F., Saavedra, R., Menichini, F., & Tezduyar, T. E. (2009). Computation of Inviscid Supersonic Flows around Cylinders and Spheres with the V-SGS Stabilization and YZβ Shock-Capturing. Journal of Applied Mechanics, 76, 021209.

[137] Corsini, A., Iossa, C., Rispoli, F., & Tezduyar, T. E. (2010). A DRD Finite Element Formulation for Computing Turbulent Reacting Flows in Gas Turbine Combustors. Computational Mechanics, 46, 159–167.

[138] Corsini, A., Rispoli, F., & Tezduyar, T. E. (2011). Stabilized Finite Element Computation of NOx Emission in Aero-engine Combustors. International Journal for Numerical Methods in Fluids, 65, 254–270.

[139] Corsini, A., Rispoli, F., & Tezduyar, T. E. (2012). Computer modeling of wave-energy air turbines with the SUPG/PSPG formulation and discontinuity-capturing technique. Journal of Applied Mechanics, 79, 010910.

[140] Corsini, A., Rispoli, F., Sheard, A. G., & Tezduyar, T. E. (2012). Computational Analysis of Noise Reduction Devices in Axial Fans with Stabilized Finite Element Formulations. Computational Mechanics, 50, 695–705.

[141] Kler, P. A., Dalcin, L. D., Paz, R. R., & Tezduyar, T. E. (2013). SUPG and

discontinuity-capturing methods for coupled fluid mechanics and electrochemical transport problems. Computational Mechanics, 51, 171–185.

[142] Corsini, A., Rispoli, F., Sheard, A. G., Takizawa, K., Tezduyar, T. E., & Venturini, P. (2014). A variational multiscale method for particle-cloud tracking in turbomachinery flows. Computational Mechanics, 54, 1191–1202.

[143] Rispoli, F., Delibra, G., Venturini, P., Corsini, A., Saavedra, R., & Tezduyar, T. E. (2015). Particle tracking and particle–shock interaction in compressible-flow computations with the V-SGS stabilization and YZβ shock-capturing. Computational Mechanics, 55, 1201–1209.

[144] Cardillo, L., Corsini, A., Delibra, G., Rispoli, F., & Tezduyar, T. E. (2016). Flow analysis of a wave-energy air turbine with the SUPG/PSPG stabilization and Discontinuity-Capturing Directional Dissipation. Computers & Fluids, 141, 184–190.

[145] Castorrini, A., Corsini, A., Rispoli, F., Venturini, P., Takizawa, K., & Tezduyar, T. E. (2016). Computational analysis of wind-turbine blade rain erosion. Computers & Fluids, 141, 175–183.

[146] Castorrini, A., Corsini, A., Rispoli, F., Venturini, P., Takizawa, K., & Tezduyar, T. E. (2019). Computational analysis of performance deterioration of a wind turbine blade strip subjected to environmental erosion. Computational Mechanics, 64, 1133–1153.

[147] Tezduyar, T. E. (2007). Finite Elements in Fluids: Stabilized Formulations and Moving Boundaries and Interfaces. Computers & Fluids, 36, 191–206.

[148] Rispoli, F., Corsini, A., & Tezduyar, T. E. (2007). Finite Element Computation of Turbulent Flows with the Discontinuity-Capturing Directional Dissipation (DCDD). Computers & Fluids, 36, 121–126.

[149] Tezduyar, T. E., & Senga, M. (2006). Stabilization and Shock-Capturing Parameters in SUPG Formulation of Compressible Flows. Computer Methods in Applied Mechanics and Engineering, 195, 1621–1632.

[150] Tezduyar, T. E., & Senga, M. (2007). SUPG Finite Element Computation of Inviscid Supersonic Flows with YZβ Shock-Capturing. Computers & Fluids, 36, 147–159.

[151] Tezduyar, T. E., Senga, M., & Vicker, D. (2006). Computation of Inviscid Supersonic Flows around Cylinders and Spheres with the SUPG Formulation and YZβ Shock-Capturing. Computational Mechanics, 38, 469–481.

[152] Tezduyar, T. E., Ramakrishnan, S., & Sathe, S. (2008). Stabilized Formulations for Incompressible Flows with Thermal Coupling. International Journal for Numerical Methods in Fluids, 57, 1189–1209.

[153] Hughes, T. J. R., Cottrell, J. A., & Bazilevs, Y. (2005). Isogeometric analysis: CAD, finite elements, NURBS, exact geometry, and mesh refinement. Computer Methods in Applied Mechanics and Engineering, 194, 4135–4195.

[154] Takizawa, K., Takagi, H., Tezduyar, T. E., & Torii, R. (2014). Estimation of Element-Based Zero-Stress State for Arterial FSI Computations. Computational Mechanics, 54, 895–910.

[155] Takizawa, K., Torii, R., Takagi, H., Tezduyar, T. E., & Xu, X. Y. (2014). Coronary arterial dynamics computation with medical-image-based time-dependent anatomical models and element-based zero-stress state estimates. Computational Mechanics, 54, 1047–1053.

[156] Takizawa, K., Tezduyar, T. E., & Sasaki, T. (2018). Estimation of element-based zero-stress state in arterial FSI computations with isogeometric wall discretization. In: Wriggers, P., & Lenarz, T. (Eds.), Biomedical Technology: Modeling, Experiments and Simulation, Lecture Notes

in Applied and Computational Mechanics. Springer, 101–122.

[157] Takizawa, K., Tezduyar, T. E., & Sasaki, T. (2017). Aorta modeling with the element-based zero-stress state and isogeometric discretization. Computational Mechanics, 59, 265–280.

[158] Sasaki, T., Takizawa, K., & Tezduyar, T. E. (2019). Aorta Zero-Stress State Modeling with T-Spline Discretization. Computational Mechanics, 63, 1315–1331.

[159] Sasaki, T., Takizawa, K., & Tezduyar, T. E. (2019). Medical-Image-Based Aorta Modeling with Zero-Stress-State Estimation. Computational Mechanics, 64, 249–271.

[160] Takizawa, K., Tezduyar, T. E., & Sasaki, T. (2019). Isogeometric hyperelastic shell analysis with out-of-plane deformation mapping. Computational Mechanics, 63, 681–700.

[161] Tezduyar, T., & Osawa, Y. (1999). Methods for Parallel Computation of Complex Flow Problems. Parallel Computing, 25, 2039–2066.

[162] Tezduyar, T., & Osawa, Y. (2001). The Multi-Domain Method for Computation of the Aerodynamics of a Parachute Crossing the Far Wake of an Aircraft. Computer Methods in Applied Mechanics and Engineering, 191, 705–716.

[163] Tezduyar, T., & Osawa, Y. (2001). Fluid–Structure Interactions of a Parachute Crossing the Far Wake of an Aircraft. Computer Methods in Applied Mechanics and Engineering, 191, 717–726.

[164] Accorsi, M. L., Leonard, J. W., Benney, R., & Stein, K. (2000). Structural Modeling of Parachute Dynamics. AIAA Journal, 38, 139–146.

[165] Tezduyar, T., Aliabadi, S., Behr, M., Johnson, A., & Mittal, S. (1993). Parallel Finite-Element Computation of 3D Flows. Computer, 26(10), 27–36.

[166] Saad, Y., & Schultz, M. (1986). GMRES: A Generalized Minimal Residual Algorithm for Solving Nonsymmetric Linear Systems. SIAM Journal of Scientific and Statistical Computing, 7, 856–869.

[167] Jonkman, J., Butterfield, S., Musial, W., & Scott, G. (2009). Definition of a 5-MW Reference Wind Turbine for Offshore System Development. Technical Report NREL/TP-500-38060, National Renewable Energy Laboratory.

[168] Gayen, B., & Sarkar, S. (2011). Direct and large-eddy simulations of internal tide generation at a near-critical slope. Journal of Fluid Mechanics, 681, 48–79.

About Authors

Kenji TAKIZAWA received his PhD from Tokyo Institute of Technology in 2005, and he is currently a Professor in Department of Modern Mechanical Engineering at Waseda University. He has been conducting computational fluid mechanics research since 2000, teaching classes on that subject since 2010, and has been conducting computational FSI research since 2003. He has published 100 Web-of-Science-indexed journal articles on computational fluid and structural mechanics and FSI. He is a Web of Science Highly Cited Researcher. He coauthored a textbook titled Computational Fluid–Structure Interaction: Methods and Applications, published by Wiley, with the Japanese translation published by Morikita Publishing Company. He served an Associate Editor of ASME Journal of Applied Mechanics and was responsible for the manuscripts on computational fluid mechanics and FSI. More information on Takizawa can be found at http://www.jp.tafsm.org/.

Yuri BAZILEVS received his PhD from University of Texas at Austin in 2006, and he is currently the E. Paul Sorensen Professor of Engineering at Brown University. He has been conducting computational fluid mechanics research since 2000, teaching classes on that subject since 2008, and has been conducting

computational FSI research since 2005. He has published over 150 Web-of-Science-indexed journal articles on computational fluid and structural mechanics and FSI. He is a Web of Science Highly Cited Researcher. He coauthored a book on isogeometric analysis, a technique widely used in computational mechanics, and FSI. He coauthored a textbook titled Computational Fluid–Structure Interaction: Methods and Applications, published by Wiley, with the Japanese translation published by Morikita Publishing Company. He is an Associate Editor of Elsevier journal Computers & Fluids and is responsible for the manuscripts on computational fluid mechanics and FSI. More information on Bazilevs can be found at https://vivo.brown.edu/display/ybazilev.

Tayfun E. TEZDUYAR received his PhD from Caltech in 1982, and he is currently the James F. Barbour Professor of Mechanical Engineering at Rice University and Professor in Faculty of Science and Engineering at Waseda University. He has been conducting computational fluid mechanics research since 1979, teaching classes on that subject since 1987, and has been conducting computational FSI research since 1991.He has published over 250 Web-of-Science-indexed journal articles on computational fluid and structural mechanics and FSI. He is a Web of Science Highly Cited Researcher. He coauthored a textbook titled Computational Fluid–Structure Interaction: Methods and Applications, published by Wiley, with the Japanese translation published by Morikita Publishing Company. He is an Editor of Springer journal Computational Mechanics and is responsible for the manuscripts on computational fluid mechanics and FSI. More information on Tezduyar can be found at http://www.tafsm.org/tezduyar/.

Artem KOROBENKO received his PhD from University of California, San Diego in 2014, and he is currently an Assistant Professor in the Department of Mechanical and Manufacturing Engineering at the University of Calgary. He has been conducting computational fluid mechanics research since 2011, teaching classes on that subject since 2016, and has been conducting computational FSI research since 2011. He has published over 20 Web-of-Science-indexed journal articles on computational fluid and structural mechanics and FSI. More information on Korobenko can be found at https://www.cfsmgroup.com/about-pi.